Sterile neutrino portal dark matter from semiproduction

Ang Liu,[1] Feng-Lan Shao,[1,*] Zhi-Long Han,[2,†] Yi Jin,[2,3] and Honglei Li[2]

[1]*School of Physics and Physical Engineering, Qufu Normal University, Qufu, Shandong 273165, China*
[2]*School of Physics and Technology, University of Jinan, Jinan, Shandong 250022, China*
[3]*Guangxi Key Laboratory of Nuclear Physics and Nuclear Technology, Guangxi Normal University, Guilin, Guangxi 541004, China*

(Received 28 August 2023; accepted 20 February 2024; published 15 March 2024)

In this paper, we study the feeble sterile neutrino portal dark matter under the Z_3 symmetry. The dark sector consists of one fermion singlet χ and one scalar singlet χ, which transform as $\chi \to e^{i2\pi/3}\chi, \phi \to e^{i2\pi/3}\phi$ under the Z_3 symmetry. Regarding fermion singlet χ as the dark matter candidate, the new interaction terms $y_\chi \phi \overline{\chi^c} \chi$ and $\mu\phi^3/2$ could induce various new production channels. For instance, when $m_\phi > 2m_\chi$, the pair decay $\phi \to \chi\chi$ could be the dominant channel, rather than the delayed decay $\phi \to \chi\nu$. Another appealing scenario is when the dark sector is initially produced through the scattering process as $NN \to \chi\chi, NN \to \phi\phi, h\nu \to \chi\phi$, then the semiproduction processes $N\chi \to \phi\phi, N\phi \to \phi\chi, N\chi \to \chi\chi$ could lead to the exponential growth of dark sector abundances. The phenomenology of the sterile neutrino and the cosmological impact of the dark scalar are also considered in the Z_3 symmetric model.

DOI: 10.1103/PhysRevD.109.055027

I. INTRODUCTION

The standard model (SM) has made great achievements in particle physics since its establishment, including but not limited to its outstanding interpretation of the basic composition of matter and successful prediction of the Higgs particle [1,2]. However, there are still some phenomena that cannot be explained by SM, e.g., the origin of tiny neutrino masses and the nature of dark matter (DM). The former is established by the discovery of neutrino oscillation [3,4], which implies that neutrino masses are below the eV scale. The latter is indicated by a variety of evidence, such as the galactic rotation curves, galaxy clusters, and large-scale structure of cosmology [5].

A natural idea is seeking a common interpretation of these two problems, which has been researched extensively [6–10]. Traditionally, high scale sterile neutrinos N are introduced to explain the tiny neutrino mass through the type-I seesaw mechanism [11,12]. If assuming sterile neutrino has keV-scale mass, it can be regarded as a decaying DM candidate [13–16]. However, the corresponding parameter space is now tightly constrained by X-ray searches [17]. One pathway to avoid such constraints is imposing additional symmetry to make the sterile neutrino a stable DM [8,18,19]. Then the sterile neutrino becomes the mediator of neutrino mass generation [20].

Despite the requirement of large Yukawa coupling and leptogenesis [21] favoring high scale sterile neutrinos, the naturalness problem suggests that sterile neutrinos should be below 10^7 GeV [22]. On the other hand, phenomenological studies usually assume that sterile neutrinos are below the TeV scale in order to be detected at colliders [23,24]. In this paper, we also consider the electroweak scale sterile neutrino. Another advantage of the low scale sterile neutrino is mediating the interaction between the dark matter and SM, which provides new annihilation or production channels of DM [25–32].

Since particle dark matter was proposed, the weakly interacting massive particle (WIMP) is the most popular candidate [33–36], which is generated through the freeze-out mechanism. Many experiments are devoted to searching for it through direct or indirect ways [37–44]. Unfortunately, there are no concrete particle DM signals that have been found so far. An alternative candidate is the feebly interacting massive particle (FIMP) [45,46], which is produced via the freeze-in mechanism. The interaction between FIMP and SM particles is so weak that it cannot reach the thermal equilibrium state. Consequently, it is produced nonthermally by the decay or annihilation of some particles in the early Universe.

The feeble sterile neutrino portal DM under the simplest Z_2 symmetry has been studied in Refs. [47–51]. In this work, we attempt to explore the generation of feeble DM via the sterile neutrino portal with the Z_3 symmetry. Within

*shaofl@mail.sdu.edu.cn
†sps_hanzl@ujn.edu.cn

the framework of the type-I seesaw, the sterile neutrino N can provide masses for SM neutrinos via the Yukawa interaction $y_\nu \overline{L}\tilde{H}N$, and couples to the dark sector. The dark sector contains a fermion singlet χ and a scalar singlet ϕ, both of which transform as $\chi \to e^{i2\pi/3}\chi, \phi \to e^{i2\pi/3}\phi$ under the exact Z_3 symmetry. Providing the mass hierarchy of dark particles as $m_\chi < m_\phi$, then the dark fermion χ becomes a DM candidate. The scenario with the strong self-interaction dark scalar ϕ and DM produced from the delayed decay $\phi \to \chi\nu$ is studied in Ref. [52]. Different from this previous study, we assume that the dark scalar ϕ is also feeble interacting with the SM. Then we perform a comprehensive investigation of freeze-in production of DM for representative scenarios. The WIMP scenario of sterile neutrino portal DM has also been studied in Ref. [53,54].

Compared with the Z_2 symmetry, the new interactions $\mu\phi^3$ and $y_\chi \phi \bar{\chi}^c \chi$ in this Z_3 symmetry will lead to new viable parameter space for DM. Recently, the semiproduction of FIMP DM has been proposed in Refs. [55,56], which can lead to the exponential growth of DM abundance. Semiproduction of sterile neutrino DM is then discussed in Ref. [57]. In this paper, we will show that the exponential growth of DM via semiproduction processes as $N\chi \to \chi\chi$, $N\chi \to \phi\phi$ and $N\phi \to \phi\chi$ is also possible in the Z_3 symmetric model.

The structure of this paper is organized as follows. In Sec. II, we briefly introduce the sterile neutrino portal DM model with the Z_3 symmetry. The evolution of feeble DM relic density for some representative scenarios is described in Sec. III. Then we analyze the constraints from testable signatures under certain scenarios in Sec. IV. Finally, discussions and conclusions are presented in Sec. V.

II. THE MODEL

The sterile neutrino portal DM further extends the SM, which includes the sterile neutrinos N_i and a dark sector with a scalar singlet ϕ and a Dirac fermion singlet χ. Among them, χ is assumed to be the FIMP DM candidate for illustration. The particle contents and the corresponding charge assignments are listed in Table I. The exact Z_3 symmetry is employed to ensure the stability of DM χ, under which the dark sector fields ϕ and χ transform nontrivially as $\phi \to e^{i2\pi/3}\phi$ and $\chi \to e^{i2\pi/3}\phi$, respectively. Yet the sterile neutrino N and SM fields transform trivially under the Z_3 symmetry. The scalar potential under the unbroken Z_3 symmetry is

$$V = -\mu_H^2 H^\dagger H + \mu_\phi^2 \phi^\dagger \phi + \lambda_H (H^\dagger H)^2 + \lambda_\phi (\phi^\dagger \phi)^2 + \lambda_{H\phi}(H^\dagger H)(\phi^\dagger \phi) + \left(\frac{\mu}{2}\phi^3 + \mathrm{H.c.}\right), \quad (1)$$

where H is the standard Higgs doublet. For simplicity, all the parameters are taken to be real. To guarantee the unbroken Z_3 symmetry, $\lambda_\phi > 0$ and $\mu_\phi > 0$ must be satisfied. After the electroweak symmetry breaking, h and ϕ can obtain physical masses,

$$m_h^2 = -2\mu_H^2, \qquad m_\phi^2 = \mu_\phi^2 + \frac{\lambda_{H\phi} v^2}{2}, \quad (2)$$

where h is identical to the 125 GeV SM Higgs boson and $v = 246$ GeV. The scalar potential is bounded below with the conditions [58]

$$\lambda_H > 0, \qquad \lambda_\phi > 0, \qquad \lambda_{H\phi} + 2\sqrt{\lambda_H \lambda_\phi} > 0. \quad (3)$$

Meanwhile, the estimation of the lifetime of the desired stable vacuum derives an upper bound on the trilinear coupling, namely, $\mu/m_\phi < 2\sqrt{\lambda_\phi}$ [59]. In the following calculation, we take $\mu = m_\phi$ and $\lambda_\phi = 1$ to meet the above inequality.

The singlet sterile neutrinos N_i not only provide mass for SM neutrinos through the type-I seesaw mechanism, but also mediate the interaction between the SM and the DM. The new Yukawa interactions and mass terms can be written as

$$-\mathcal{L}_Y \supset \left(y_\nu \bar{L}\tilde{H}N + y_N \phi\bar{\chi}N + \frac{1}{2} m_N \overline{N^c} N + \mathrm{H.c.}\right) + y_\chi \phi \overline{\chi^c}\chi + m_\chi \bar{\chi}\chi, \quad (4)$$

where $\tilde{H} = i\sigma_2 H^*$. The tiny neutrino mass is generated via the first item, and can be expressed as

$$m_\nu = -\frac{v^2}{2} y_\nu m_N^{-1} y_\nu^T. \quad (5)$$

In order to explain the neutrino oscillation data, at least two sterile neutrinos $N_i (i = 1, 2, \ldots)$ are required [60]. Adopting the Casas-Ibarra parametrization [61], the Yukawa coupling y_ν can be expressed as

$$y_\nu = \frac{\sqrt{2}}{v} U_{\mathrm{PMNS}} \hat{m}_\nu^{1/2} R\, \hat{m}_N^{1/2}, \quad (6)$$

where $\hat{m}_\nu$ and $\hat{m}_N$ are the diagonalized mass matrices for active and sterile neutrinos, and U_{PMNS} is the mixing matrix for active neutrinos. R is a generalized orthogonal matrix.

TABLE I. Relevant particle contents and the corresponding charge assignments under the Z_3 symmetry. Here $\omega \equiv e^{i2\pi/3}$.

	L	N	χ	H	ϕ
$SU(2)_L$	2	1	1	2	1
$U(1)_Y$	$-\frac{1}{2}$	0	0	$\frac{1}{2}$	0
Z_3	1	1	ω	1	ω

For the simplest seesaw with two sterile neutrinos, R is determined by a rotation matrix with a complex angle ξ [60]. Under the constraints from lepton flavor violation, $\mathrm{Im}(\xi) < 7$ is required [62]. The mixing matrix between the active and sterile neutrinos can be calculated as

$$\theta = \frac{y_\nu v}{\sqrt{2}} \hat{m}_N^{-1} = U_{\mathrm{PMNS}} \hat{m}_\nu^{1/2} R \, \hat{m}_N^{-1/2}. \tag{7}$$

For illustration, we consider the normal hierarchy of neutrino masses. The lightest neutrino ν_1 is massless with two sterile neutrinos introduced. The masses of the other two heavier active neutrinos m_{ν_2}, m_{ν_3}, the three neutrino mixing angles $\theta_{12}, \theta_{13}, \theta_{23}$, and the Dirac phase δ are fixed to the best fit value [63]. Meanwhile, the Majorana phases α_1, α_2 are set to be zero. The explicit values are

$$\begin{gathered} m_{\nu_1} = 0 \text{ eV}, \qquad m_{\nu_2} = 8.6 \times 10^{-3} \text{ eV}, \qquad m_{\nu_3} = 5.0 \times 10^{-2} \text{ eV}, \\ \theta_{12} = 33.44^\circ, \qquad \theta_{13} = 8.57^\circ, \qquad \theta_{23} = 49.2^\circ, \qquad \delta = 197^\circ, \qquad \alpha_1 = \alpha_2 = 0. \end{gathered} \tag{8}$$

In this paper, we fix $\mathrm{Re}(\xi) = 0.1$ and vary $0 < \mathrm{Im}(\xi) < 7$ to obtain relatively large elements of mixing matrix θ for phenomenology discussion. We also assume a hierarchical mass spectrum of the sterile neutrinos, i.e., $m_{N_2} = 10 m_{N_1}$. In this way, the Yukawa coupling y_ν and mixing matrix θ are determined by the parameter m_{N_1} and $\mathrm{Im}(\xi)$. Focusing on the DM phenomenology, it is enough to consider that the DM exclusively couples to the lightest sterile neutrino N_1. For simplicity, we use the notation $N \equiv N_1$ in the following discussions.

III. RELIC DENSITY

We consider the fermion singlet χ as the FIMP DM candidate in this paper. The dark scalar singlet ϕ is also assumed feeble interacting with SM, and is lighter than the sterile neutrino. Meanwhile, the electroweak scale sterile neutrino N is always in thermal equilibrium via neutrino oscillation [64] or additional interactions [65]. The generation of dark scalar ϕ is relatively simple, including the Higgs portal annihilation $\mathrm{SM} \to \phi\phi$, the sterile neutrino portal direct decay $N \to \phi\chi$, scattering process $h\nu \to \chi\phi$, $hN \to \chi\phi$, pair annihilation $NN \to \phi\phi$, and semiproduction $N\chi \to \phi\phi$. As for fermion DM χ, it can be produced through plenty of processes, such as direct decay $N \to \phi\chi$, delayed decay $\phi \to \chi\nu$, pair decay $\phi \to \chi\chi$, pair production $NN \to \chi\chi$, semiproduction $N\chi \to \chi\chi$, $N\phi \to \phi\chi$, conversion processes $\phi\phi \to \chi\chi$, and so on. In addition to the pair decay $\phi \to \chi\chi$, the semiproduction processes $N\chi \to \chi\chi$, $N\chi \to \phi\phi$, and $N\phi \to \phi\chi$ are new in this Z_3 symmetric model. Typical Feynman diagrams for dark sector generation and conversion are shown in Figs. 1 and 2. For simplicity, we neglect those channels with petty influences of the relic density of the dark sector, e.g., $h\phi \to \phi\phi$, $h\phi \to \chi\chi$. The relevant Boltzmann equations describing the evolution of dark sector abundances are given by

$$\begin{aligned} \frac{dY_\phi}{dz} = {} & \frac{k}{z^2} \langle \sigma v \rangle_{h\nu \to \chi\phi} \left(Y_h^{\mathrm{eq}} Y_\nu^{\mathrm{eq}} - \frac{Y_h^{\mathrm{eq}} Y_\nu^{\mathrm{eq}}}{Y_\chi^{\mathrm{eq}} Y_\phi^{\mathrm{eq}}} Y_\chi Y_\phi \right) + \frac{k}{z^2} \langle \sigma v \rangle_{Nh \to \chi\phi} \left(Y_N^{\mathrm{eq}} Y_h^{\mathrm{eq}} - \frac{Y_N^{\mathrm{eq}} Y_h^{\mathrm{eq}}}{Y_\chi^{\mathrm{eq}} Y_\phi^{\mathrm{eq}}} Y_\chi Y_\phi \right) \\ & + \frac{k}{z^2} \langle \sigma v \rangle_{\mathrm{SM} \to \phi\phi} \left((Y_{\mathrm{SM}}^{\mathrm{eq}})^2 - \left(\frac{Y_{\mathrm{SM}}^{\mathrm{eq}}}{Y_\phi^{\mathrm{eq}}} \right)^2 Y_\phi^2 \right) + \frac{k}{z^2} \langle \sigma v \rangle_{NN \to \phi\phi} \left((Y_N^{\mathrm{eq}})^2 - \left(\frac{Y_N^{\mathrm{eq}}}{Y_\phi^{\mathrm{eq}}} \right)^2 Y_\phi^2 \right) \\ & + k^\star z \tilde{\Gamma}_{N \to \phi\chi} \left(Y_N^{\mathrm{eq}} - \frac{Y_N^{\mathrm{eq}}}{Y_\phi^{\mathrm{eq}} Y_\chi^{\mathrm{eq}}} Y_\phi Y_\chi \right) + \frac{k}{z^2} \langle \sigma v \rangle_{N\chi \to \phi\phi} \left(Y_N^{\mathrm{eq}} Y_\chi - \frac{Y_N^{\mathrm{eq}} Y_\chi^{\mathrm{eq}}}{(Y_\phi^{\mathrm{eq}})^2} Y_\phi^2 \right) \\ & - \frac{k}{z^2} \langle \sigma v \rangle_{\phi\phi \to \chi\chi} \left(Y_\phi^2 - \left(\frac{Y_\phi^{\mathrm{eq}}}{Y_\chi^{\mathrm{eq}}} \right)^2 Y_\chi^2 \right) - k^\star z \tilde{\Gamma}_{\phi \to \chi\nu} \left(Y_\phi - \frac{Y_\phi^{\mathrm{eq}}}{Y_\chi^{\mathrm{eq}}} Y_\chi \right) \\ & - k^\star z \tilde{\Gamma}_{\phi \to \chi\chi} \left(Y_\phi - \frac{Y_\phi^{\mathrm{eq}}}{(Y_\chi^{\mathrm{eq}})^2} Y_\chi^2 \right) \end{aligned} \tag{9}$$

$$\begin{aligned} \frac{dY_\chi}{dz} = {} & \frac{k}{z^2} \langle \sigma v \rangle_{h\nu \to \chi\phi} \left(Y_h^{\mathrm{eq}} Y_\nu^{\mathrm{eq}} - \frac{Y_h^{\mathrm{eq}} Y_\nu^{\mathrm{eq}}}{Y_\chi^{\mathrm{eq}} Y_\phi^{\mathrm{eq}}} Y_\chi Y_\phi \right) + \frac{k}{z^2} \langle \sigma v \rangle_{Nh \to \chi\phi} \left(Y_N^{\mathrm{eq}} Y_h^{\mathrm{eq}} - \frac{Y_N^{\mathrm{eq}} Y_h^{\mathrm{eq}}}{Y_\chi^{\mathrm{eq}} Y_\phi^{\mathrm{eq}}} Y_\chi Y_\phi \right) \\ & + \frac{k}{z^2} \langle \sigma v \rangle_{NN \to \chi\chi} \left((Y_N^{\mathrm{eq}})^2 - \frac{(Y_N^{\mathrm{eq}})^2}{(Y_\chi^{\mathrm{eq}})^2} Y_\chi^2 \right) + \frac{k}{z^2} \langle \sigma v \rangle_{N\phi \to \phi\chi} \left(Y_N^{\mathrm{eq}} Y_\phi - \frac{Y_N^{\mathrm{eq}}}{Y_\chi^{\mathrm{eq}}} Y_\phi Y_\chi \right) \end{aligned}$$

$$+\frac{k}{z^2}\langle\sigma v\rangle_{N\chi\to\chi\chi}\left(Y_N^{\rm eq}Y_\chi-\frac{Y_N^{\rm eq}}{Y_\chi^{\rm eq}}Y_\chi^2\right)-\frac{k}{z^2}\langle\sigma v\rangle_{N\chi\to\phi\phi}\left(Y_N^{\rm eq}Y_\chi-\frac{Y_N^{\rm eq}Y_\chi^{\rm eq}}{(Y_\phi^{\rm eq})^2}Y_\phi^2\right)$$
$$+\frac{k}{z^2}\langle\sigma v\rangle_{\phi\phi\to\chi\chi}\left(Y_\phi^2-\left(\frac{Y_\phi^{\rm eq}}{Y_\chi^{\rm eq}}\right)^2Y_\chi^2\right)+k^\star z\tilde{\Gamma}_{N\to\phi\chi}\left(Y_N^{\rm eq}-\frac{Y_N^{\rm eq}}{Y_\phi^{\rm eq}Y_\chi^{\rm eq}}Y_\phi Y_\chi\right)$$
$$+k^\star z\tilde{\Gamma}_{\phi\to\chi\nu}\left(Y_\phi-\frac{Y_\phi^{\rm eq}}{Y_\chi^{\rm eq}}Y_\chi\right)+2k^\star z\tilde{\Gamma}_{\phi\to\chi\chi}\left(Y_\phi-\frac{Y_\phi^{\rm eq}}{(Y_\chi^{\rm eq})^2}Y_\chi^2\right), \tag{10}$$

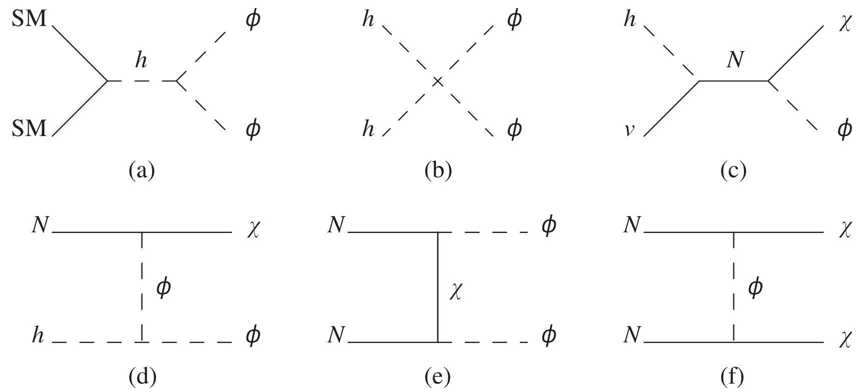

FIG. 1. Typical Feynman diagrams for the dark sector generation, which also appear in the Z_2 symmetric model. The generation of dark particles from the SM particle annihilation processes (panels (a),(b)), from the scattering processes (panels (c),(d)), and from the sterile neutrino annihilation processes (panels (e),(f)).

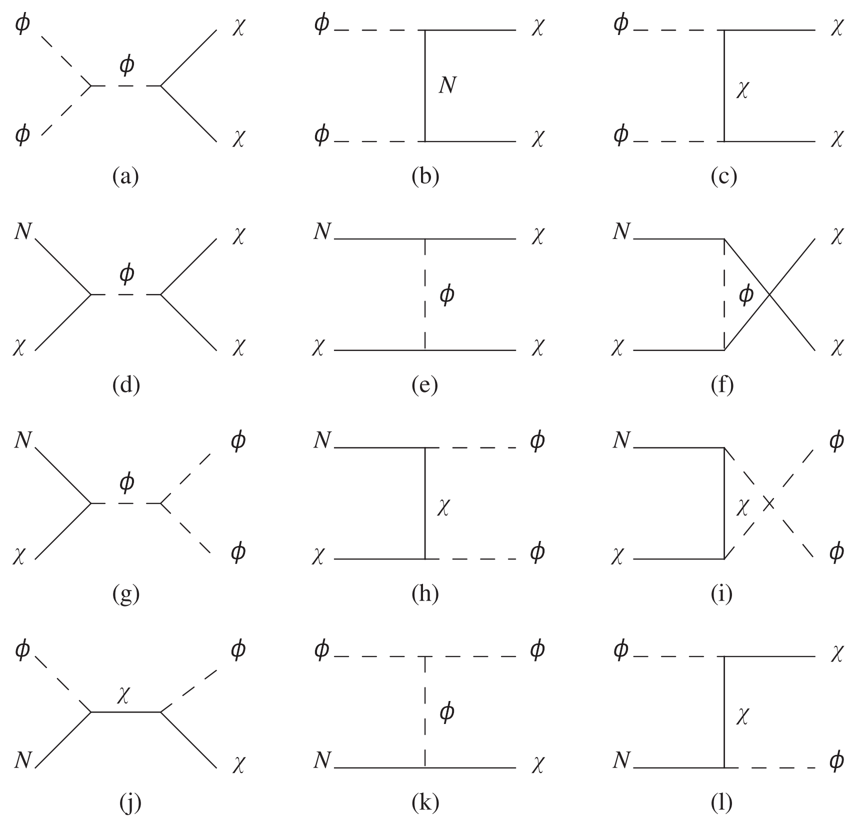

FIG. 2. Feynman diagrams for the conversion processes $\phi\phi\to\chi\chi$ (panels (a)–(c)), and various semi-production processes $N\chi\to\chi\chi$ (panels (d)–(f)), $N\chi\to\phi\phi$ (panels (g)–(i)), and $N\phi\to\phi\chi$ (panels (j)–(l)).

TABLE II. The parameter choices for scenario 1, the units of masses involved are GeV.

Scenario 1	m_χ	m_ϕ	m_N	y_N	y_χ	$\lvert y_{\nu 1}\rvert$	$\lambda_{H\phi}$	μ	$\mathrm{Im}(\xi)$
a	10	15	50	10^{-13}	10^{-12}	4×10^{-5}	6.7×10^{-12}	15	5.55
b	10	15	50	10^{-13}	2×10^{-3}	2×10^{-6}	6.7×10^{-12}	15	2.56
c	10	15	50	3.7×10^{-12}	10^{-12}	3×10^{-6}	10^{-14}	15	2.96
d	10	15	50	3.7×10^{-12}	2×10^{-3}	10^{-6}	10^{-14}	15	1.88

where we use the definition $z \equiv m_\chi/T$, and T is the temperature. The parameters k and $k^\star$ are defined as $k = \sqrt{\pi g_\star/45}\, m_\chi M_{\rm Pl}$ and $k^* = \sqrt{45/4\pi^3 g_\star}\, M_{\rm Pl}/m_\chi^2$ respectively, where $g_\star$ is the effective number of degrees of freedom of the relativistic species and $M_{\rm Pl} = 1.2\times 10^{19}$ GeV is the Planck mass. The thermal decay width $\tilde{\Gamma}_i$ is calculated as $\Gamma_i \mathcal{K}_1/\mathcal{K}_2$ with $\mathcal{K}_{1,2}$ being the first and second modified Bessel function of the second kind.

The corresponding decay widths are given by

$$\Gamma_{N\to\chi\phi} = \frac{y_N^2}{16\pi m_N}\left(\frac{(m_N+m_\chi)^2 - m_\phi^2}{m_N^2}\right) \times \lambda^{1/2}({m_N}^2, {m_\phi}^2, {m_\chi}^2), \tag{11}$$

$$\Gamma_{\phi\to\chi\nu} = \frac{y_N^2 |y_{\nu 1}|^2 v^2 m_\phi}{16\pi m_N^2}\left(\frac{m_\phi^2 - m_\chi^2}{m_\phi^2}\right)^2, \tag{12}$$

$$\Gamma_{\phi\to\chi\chi} = \frac{y_\chi^2}{4\pi m_\phi^2}(m_\phi^2 - 4m_\chi^2)^{3/2}, \tag{13}$$

where $|y_{\nu 1}|^2 = |(y_\nu)_{e1}|^2 + |(y_\nu)_{\mu 1}|^2 + |(y_\nu)_{\tau 1}|^2$, the kinematic function $\lambda(a,b,c)$ is defined as

$$\lambda(a,b,c) = a^2 + b^2 + c^2 - 2ab - 2ac - 2bc. \tag{14}$$

Moreover, the thermal average cross sections $\langle\sigma v\rangle$ are calculated numerically by micrOMEGAs [66]. For the feeble dark sector, the above Boltzmann equations are solved with the initial condition $Y_\chi = Y_\phi = 0$. To avoid possible double counting of generated on-shell particles in the s channel, we also apply the real intermediate states subtraction [67]. In the above Boltzmann equations, the dark sector distribution functions following the equilibrium behavior are assumed. More precise calculations involving semiproduction processes can be found in Ref. [68].

The various production channels for DM χ in this Z_3 symmetric model heavily depend on the masses of the dark sector and sterile neutrino. Depending on whether the decays $N\to\phi\chi$ and $\phi\to\chi\chi$ are kinematically allowed, we classify the mass spectrum into four scenarios, namely, (1) $m_N > m_\phi + m_\chi$ with $m_\phi < 2m_\chi$, (2) $m_N > m_\phi + m_\chi$ with $m_\phi > 2m_\chi$, (3) $m_N < m_\phi + m_\chi$ with $m_\phi < 2m_\chi$, and (4) $m_N < m_\phi + m_\chi$ with $m_\phi > 2m_\chi$, where for the latter two scenarios $m_\phi < m_N$ is also satisfied. Theoretically, there are also four scenarios when $m_\phi > m_N$. By replacing the contribution of $N\to\phi\chi$ with $\phi\to N\chi$, we find that the results for $m_\phi > m_N$ scenarios are quite similar to the $m_\phi < m_N$ scenarios, so we will not repeat the $m_\phi > m_N$ scenarios in this paper.

In the following study, we additionally calculate the results under the Z_2 symmetry for comparison. Specifically, we give priority to considering benchmark points under the Z_3 symmetry to meet the Planck observed relic density $\Omega_{\rm DM}h^2 = 0.12$ [69], whereupon use the parameters occurring under the Z_2 symmetry at the same time, i.e., $\{m_\chi, m_\phi, m_N, y_N, y_\nu, \lambda_{H\phi}\}$, to calculate the abundances of dark particles. In addition, the mass of DM is fixed as 10 GeV for illustration.

A. Scenario 1

In scenario 1, we consider that the direct decay $N\to\phi\chi$ is opened, while the pair decay $\phi\to\chi\chi$ is prohibited. The production of dark scalar can be classified into two kinds of process. One is the SM Higgs portal through the coupling $\lambda_{H\phi}$, and the other one is the sterile neutrino portal via the coupling y_N. Meanwhile, the new Yukawa coupling y_N contributes to the conversion processes as shown in Fig. 2. To illustrate the impact of these conditions, we select four sets of parameters in Table II. The corresponding evolution of Y_ϕ and Y_χ is shown in Fig. 3.

In scenario 1(a), we choose the Higgs portal coupling $\lambda_{H\phi}$, which is much larger than the sterile neutrino portal coupling y_N. In this way, the dark scalar ϕ is dominantly generated through the process SM $\to\phi\phi$, and the decay channel $N\to\phi\chi$ is subdominant. Because of the relatively tiny y_N and y_χ, the DM abundance Y_χ from direct decay $N\to\phi\chi$ is miserly; meanwhile contributions from the other $2\to 2$ scattering processes are also negligible. With the cross section $\langle\sigma v\rangle_{{\rm SM}\to\phi\phi} \simeq 3.9\times10^{-45}$ cm^3/s, the Planck observed DM abundance is generated via SM $\to\phi\phi$ followed by the delayed decay $\phi\to\chi\nu$. In Fig. 3(a), we can see that the evolution of Y_χ and Y_ϕ are consistent in the Z_2 and Z_3 symmetries all the time; thus, R_χ equals one invariably. This is because of the same generation pattern for the dark sector with only $\phi\to\chi\nu$ allowed in this scenario.

In scenario 1(b), the value of y_χ is increased to 2×10^{-3} compared with scenario 1(a), meanwhile, the other parameters are kept the same. As shown in Fig. 2, there are new

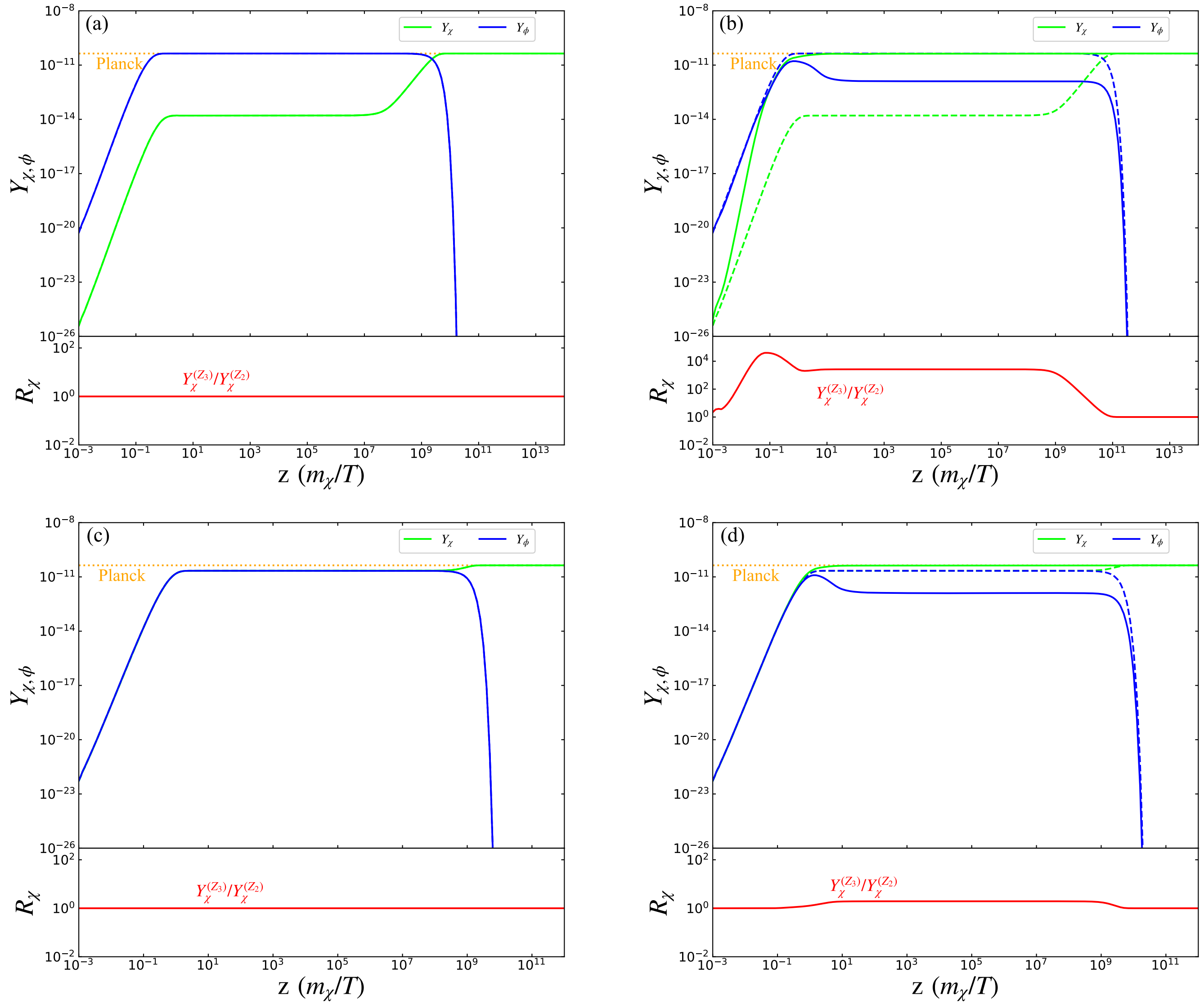

FIG. 3. The evolution of dark sector abundances Y_χ (green), Y_ϕ (blue), and the ratio R_χ (red) in scenario 1. The solid lines represent the evolution of the dark sector under Z_3 symmetry, while the dashed lines are for the Z_2 symmetry. The ratio R_χ equals $Y_\chi^{(Z_3)}/Y_\chi^{(Z_2)}$, where $Y_\chi^{(Z_3)}$ and $Y_\chi^{(Z_2)}$ are the abundance of DM χ under the Z_3 and the Z_2 symmetries, respectively. The orange dotted lines are the Planck observed relic density for $m_\chi = 10$ GeV. Panels (a), (b), (c) and (d) correspond to the four cases in Table II respectively.

s-channel and t-channel contributions to the conversion process $\phi\phi \to \chi\chi$ under the Z_3 symmetry which do not involve the coupling y_N. Different from the $\phi\phi \to \chi\chi$ process, the other conversion processes are suppressed by the smallness of y_N. The corresponding cross section $\langle\sigma v\rangle_{\phi\phi\to\chi\chi} = 1.1 \times 10^{-25}$ cm^3/s has been greatly enhanced for this scenario, which causes the transition of dark scalar ϕ into DM χ. The results are shown in panel (b) of Fig. 3, where Y_χ is increased by a factor of 2.6×10^3 before ϕ decays compared with the Z_2 case. According to our calculation, the conversion becomes significant when $y_\chi \gtrsim 10^{-4}$, i.e., the cross section $\langle\sigma v\rangle_{\phi\phi\to\chi\chi} \gtrsim 2.7 \times 10^{-28}$ cm^3/s. The conversion effect leads to the production of DM χ earlier than the Z_2 case. Afterwards, the ratio R_χ remains on a downward trend until it becomes a constant after ϕ totally freeze-in. The value of this constant is proportional to the conversion rate $\langle\sigma v\rangle_{\phi\phi\to\chi\chi}$. In this scenario, the dark scalar ϕ is mainly produced via the process SM $\to \phi\phi$ as in scenario 1(a), so the same amount of abundance Y_ϕ is expected provided the absence of conversion $\phi\phi \to \chi\chi$, which leads to a final reduction of R_χ to one after the scalar decays via $\phi \to \chi\nu$.

In scenario 1(c), we consider the opposite case with $\lambda_{H\phi} \ll y_N$. For $\lambda_{H\phi} = 10^{-14}$, the Higgs portal process SM $\to \phi\phi$ is heavily suppressed, so is the other $2 \to 2$ scattering processes with $y_N \sim y_\chi \sim 10^{-12}$. The direct decay $N \to \phi\chi$ becomes the dominant contribution of Y_ϕ and Y_χ,

TABLE III. The parameter choices for the four cases in scenario 2, the units of masses involved are GeV.

Scenario 2	m_χ	m_ϕ	m_N	y_N	y_χ	$\lvert y_{\nu 1}\rvert$	$\lambda_{H\phi}$	μ	$\mathrm{Im}(\xi)$
a	10	25	40	10^{-13}	10^{-12}	7×10^{-7}	4.8×10^{-12}	25	1.64
b	10	25	40	10^{-13}	1.2×10^{-4}	5×10^{-6}	3.9×10^{-12}	25	3.58
c	10	25	40	3.7×10^{-12}	10^{-12}	10^{-6}	10^{-14}	25	1.98
d	10	25	40	3.7×10^{-12}	1.2×10^{-4}	8×10^{-7}	10^{-14}	25	1.77

which leads to $Y_\phi = Y_\chi$ at the beginning. The final abundance of dark scalar is then converted into DM via the delayed decay $\phi \to \chi\nu$. In this scenario, the ratio R_χ equals to one all the time as shown in Fig. 3(c).

In scenario 1(d), the conversion process $\phi\phi \to \chi\chi$ is also enhanced with relatively large y_χ. Although the strong conversion process does not affect the evolution of the dark sector at the very beginning, it can convert ϕ into χ around the time of DM freeze-in, which increases R_χ to 2. Compared to the Z_2 case, Y_χ satisfies the Planck constraint much earlier in the Z_3 symmetry. R_χ decreases to 1 after the decay of dark scalar ϕ.

Based on the above results, we can conclude that when the direct decay $N \to \phi\chi$ is allowed and the delayed decay $\phi \to \chi\nu$ is the only decay mode of dark scalar, the final DM abundance in the Z_3 symmetric model is the same as in the Z_2 symmetric model, although the conversion process $\phi\phi \to \chi\chi$ could impact the evolution of DM. So in scenario 1, we cannot directly distinguish the Z_3 symmetry from the Z_2 symmetry only through the final relic density. However there is improvement in phenomenology due to different Y_ϕ evolution in scenarios 1(b) and 1(d).

B. Scenario 2

For scenario 2, we increase the mass of the dark scalar to open the pair decay $\phi \to \chi\chi$, while keeping the decay of $N \to \phi\chi$ allowed. Because the delayed decay $\phi \to \chi\nu$ is further suppressed by the small mixing parameter θ, the pair decay $\phi \to \chi\chi$ is the dominant mode even with $y_N \simeq y_\chi$. Four sets of parameters are chosen in Table III. Although the generation mode of the dark scalar ϕ in scenario 2 is consistent with the corresponding cases in scenario 1, the final conversion of $\phi \to \chi$ is significantly different. Fig. 4 shows the corresponding evolution of dark particles.

In scenario 2(a), the contributions from direct decay $N \to \phi\chi$ to the dark sector abundances are tiny. The dark scalar ϕ is dominantly produced from SM $\to \phi\phi$. The correct abundance Y_χ is obtained with $\langle\sigma v\rangle_{\mathrm{SM}\to\phi\phi} \simeq 2\times10^{-45}\ \mathrm{cm}^3/\mathrm{s}$ followed by the pair decay $\phi \to \chi\chi$. The conversion of $\phi \to \chi$ happens much earlier than the Z_2 symmetric model due to $\Gamma_{\phi\to\chi\chi} \gg \Gamma_{\phi\to\chi\nu}$. The ratio R_χ equals one before ϕ decays, and quickly increases to 4.1×10^3 after ϕ decays. Since this pair decay converts one ϕ into two χ, the observed DM abundance Y_χ^{obs} is realized with $Y_\phi(z=10) = Y_\chi^{\mathrm{obs}}/2$ in the Z_3 symmetric model. In the Z_2 symmetric model, the conversion is via the delayed decay $\phi \to \chi\nu$, which leads to $Y_\chi(z=\infty) = Y_\phi(z=10) = Y_\chi^{\mathrm{obs}}/2$. So the final ratio R_χ is two in scenario 2(a).

In scenario 2(b), the relatively large y_χ not only enhances the conversion rate of $\phi\phi \to \chi\chi$, but also increases the decay width $\Gamma_{\phi\to\chi\chi}$. Our numerical calculation finds that compared with scenario 2(a), a slightly smaller $\lambda_{H\phi}$ with $\langle\sigma v\rangle_{\mathrm{SM}\to\phi\phi} \simeq 1.3\times10^{-45}\ \mathrm{cm}^3/\mathrm{s}$ could satisfy the Planck constraint. Once produced, the dark scalar decays quite quickly into a DM pair, which results in $Y_\phi \ll Y_\chi$. The inverse conversion process and the fast pair decay transform a small part of the dark sector as $2\chi \to 2\phi \xrightarrow{\mathrm{decay}} 4\chi$, which makes the generation of DM more efficient in this scenario. The ratio R_χ decreases during the evolution, and finally R_χ reaches about 3.1 in scenario 2(b).

In scenario 2(c), the dark sector abundances Y_ϕ and Y_χ are initially produced via the direct decay $N \to \phi\chi$. Then the dark scalar ϕ is converted to DM χ by the pair decay $\phi \to \chi\chi$. The cascade decay chain is $N \to \phi\chi \to \chi\chi\chi$ in the Z_3 symmetric model. Under the Z_2 symmetry, the decay chain is $N \to \phi\chi \to \chi\nu\chi$. So as shown in Fig. 4(c), the ratio R_χ increases to 3 after ϕ decays in the Z_3 symmetric model, and then decreases to $3/2$ after ϕ decays in the Z_2 symmetric model.

In scenario 2(d), the initial dark sector abundances from $N \to \phi\chi$ decay are much smaller than in scenario 2(b), so the contribution from the conversion process $\phi\phi \to \chi\chi$ is too small to make Y_χ exceed obviously even with the same y_N. Therefore, the increase of R_χ in the early stage is mainly determined by $\phi \to \chi\chi$. The final ratio R_χ is also $3/2$ in scenario 2(d).

The new pair decay $\phi \to \chi\chi$ makes the Z_3 symmetric model different from the Z_2 symmetric model. With the same couplings in the Z_3 symmetric model, the generated DM abundance in the Z_2 symmetric model is always smaller than the observed value. Depending on the dominant generation process of dark scalar, the ratio R_χ is also different. When the dark scalar is dominantly produced via the Higgs portal SM $\to \phi\phi$, the final ratio is $R_\chi \gtrsim 2$. Meanwhile, if the dark scalar is generated from direct decay $N \to \phi\chi$, the predicted final ratio is $R_\chi = 3/2$. The dark scalar is short lived in the Z_3 symmetric model due to the relatively large partial decay width $\Gamma_{\phi\to\chi\chi}$. Then the tight constraints from cosmology can be easily satisfied in scenario 2.

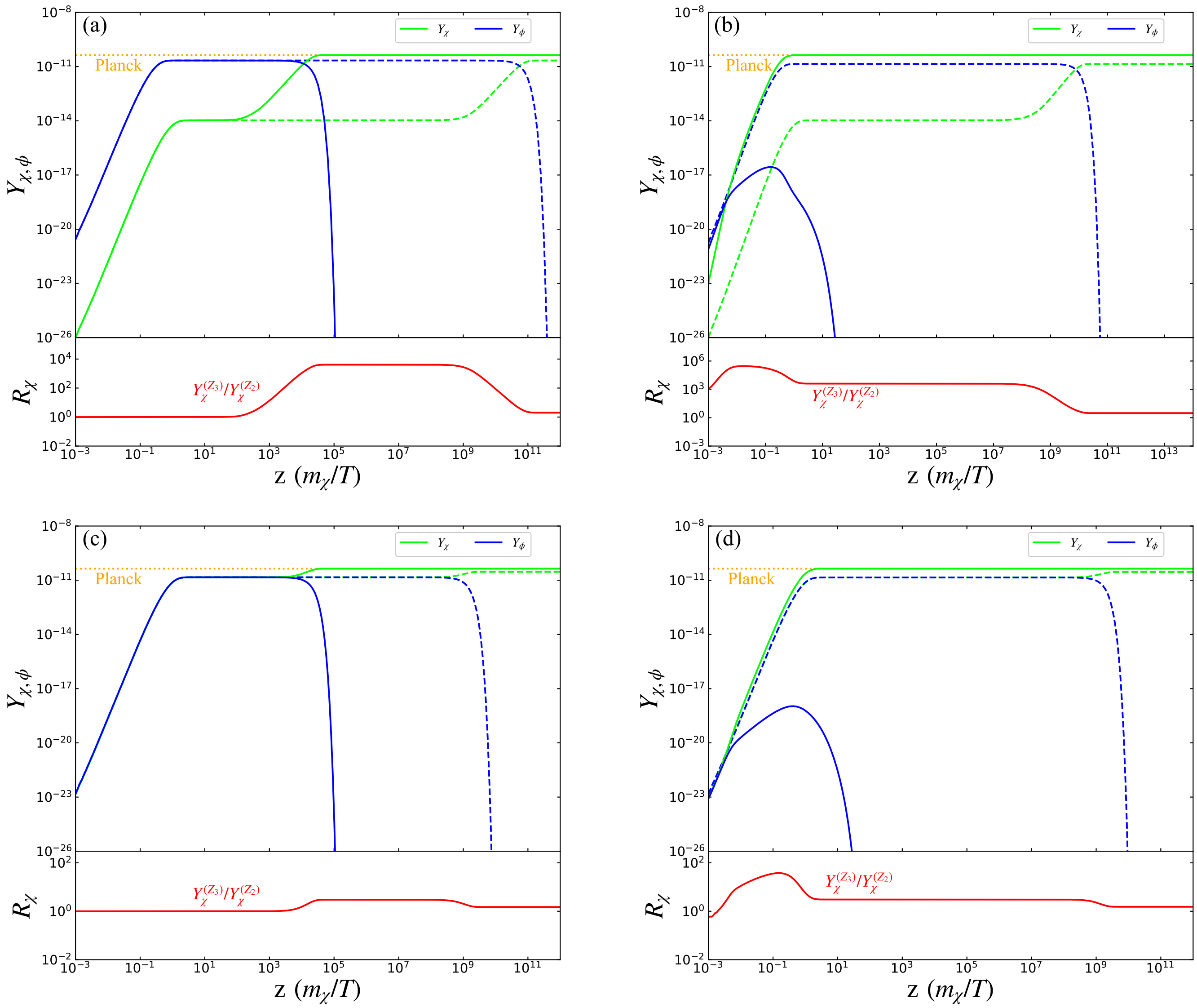

FIG. 4. Same as Fig. 3, but for scenario 2. Panels (a), (b), (c) and (d) correspond to the four cases in Table III respectively

C. Scenario 3

The sterile neutrino portal coupling y_N is at the order of $\mathcal{O}(10^{-13})$ aiming not to exceed the observed DM relic abundance from direct decay $N \to \phi\chi$ in the previous two scenarios. In scenario 3, we consider that both decay modes $N \to \phi\chi$ and $\phi \to \chi\chi$ are prohibited kinematically. Compared to the previous two scenarios, the $2 \to 2$ scattering channels as $NN \to \chi\chi$ and $h\nu \to \chi\phi$ will dominate the production of χ at the very beginning in this scenario. Besides the Higgs portal SM $\to \phi\phi$ channels, the other scattering processes can also make considerable contributions to the production of ϕ. We take four sets of parameters in Table IV to illustrate this scenario. In addition, the evolution of the abundance of dark particles is shown in Fig. 5.

In scenario 3(a), the dark scalar ϕ is dominantly produced via SM $\to \phi\phi$. With $\langle\sigma v\rangle_{\mathrm{SM}\to\phi\phi} \simeq 3.9 \times 10^{-45}\ \mathrm{cm}^3/\mathrm{s}$,

TABLE IV. The parameter choices for the four cases in scenario 3, the units of masses involved are GeV.

Scenario 3	m_χ	m_ϕ	m_N	y_N	y_χ	$\lvert y_{\nu 1}\rvert$	$\lambda_{H\phi}$	μ	$\mathrm{Im}(\xi)$
a	10	14	20	10^{-13}	10^{-12}	3×10^{-5}	6.6×10^{-12}	14	5.72
b	10	14	20	10^{-13}	2×10^{-3}	10^{-6}	6.6×10^{-12}	14	2.32
c	10	14	20	1.6×10^{-7}	10^{-12}	7×10^{-7}	10^{-14}	14	1.97
d	10	14	20	6×10^{-8}	5.7×10^{-1}	8×10^{-7}	10^{-14}	14	2.10

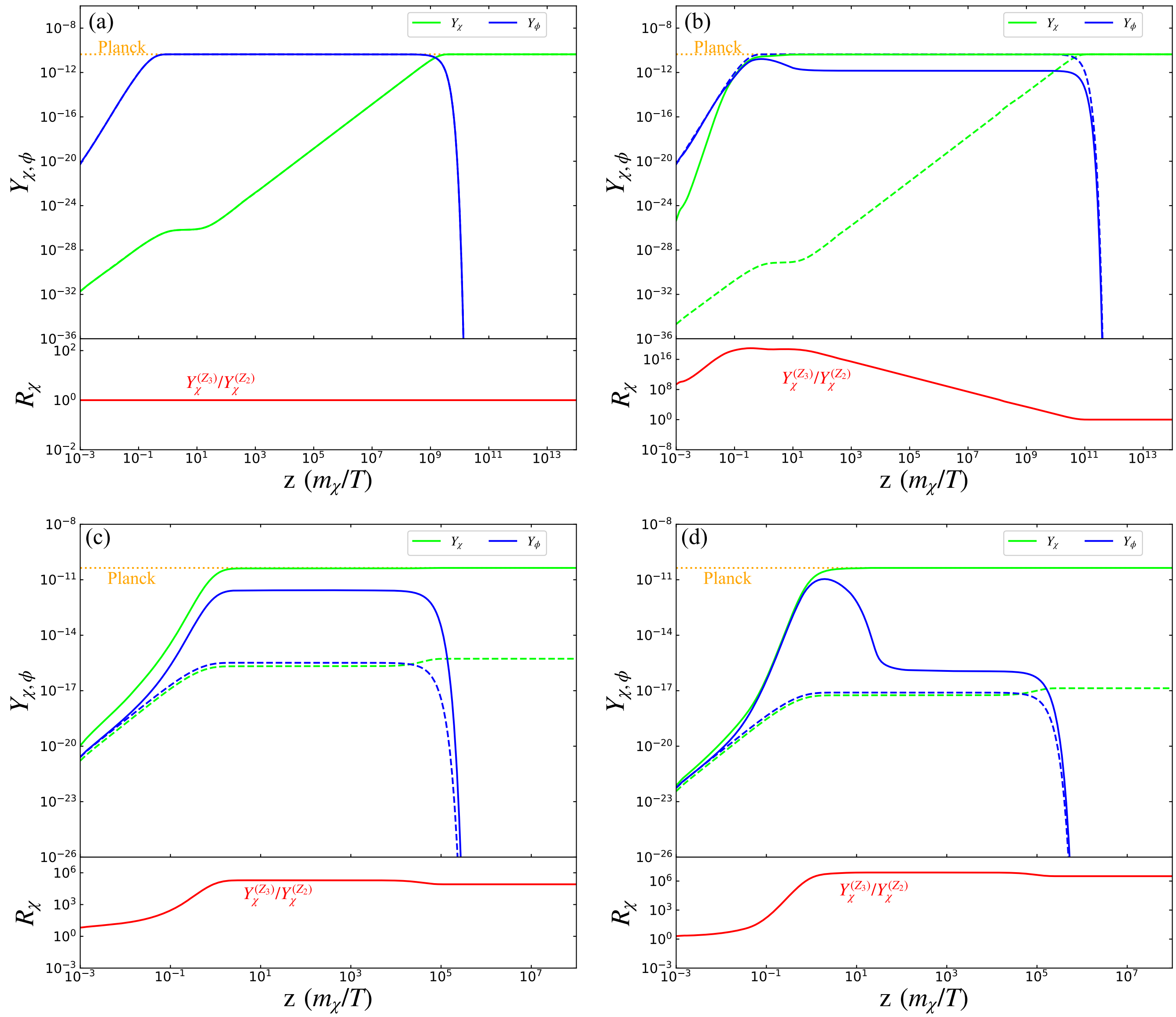

FIG. 5. Same as Fig. 3, but for scenario 3. Panels (a), (b), (c) and (d) correspond to the four cases in Table IV respectively

correct DM relic abundance Y_χ is obtained by delayed decay $\phi \to \chi\nu$. It is obvious in Fig. 5(a) that the contribution from scattering to the generation of DM χ is much lower than that from $N \to \phi\chi$ decay. With the lighter m_ϕ, a slightly smaller $\lambda_{H\phi}$ is required compared with scenario 1(a). The ratio R_χ is invariant to one due to the same transformation process under the two symmetries.

In scenario 3(b), the conversion process $\phi\phi \to \chi\chi$ is enhanced, which becomes the dominant production mode of χ. The large conversion rate leads R_χ to rise to an enormous value $\sim\mathcal{O}(10^{18})$ in the initial time, and then decreases to one with the completion of $\phi \to \chi\nu$.

In scenario 3(c), the contribution of SM $\to \phi\phi$ can be ignored due to tiny $\lambda_{H\phi}$. The dark sector is primarily generated by scattering processes as $NN \to \chi\chi$, $NN \to \phi\phi$, $h\nu \to \chi\phi$ at the very beginning. The typical scattering cross sections are $\langle\sigma v\rangle_{NN\to\chi\chi} \simeq 1.9 \times 10^{-48}$ cm^3/s, $\langle\sigma v\rangle_{NN\to\phi\phi} \simeq 3.0 \times 10^{-48}$ cm^3/s, and $\langle\sigma v\rangle_{h\nu\to\chi\phi} \simeq 3.0 \times 10^{-49}$ cm^3/s for the benchmark point. It can be seen from Fig. 5(c) that the generated dark abundances from scattering are 5 orders of magnitudes lower than the observed value under the Z_2 symmetry. Nevertheless, the new semiproduction processes $N\chi \to \phi\phi$ and $N\phi \to \phi\chi$ are enhanced with $\mu = m_\phi$ and $y_N = 1.6 \times 10^{-7}$ under the Z_3 symmetry, which results in the exponential growth of dark sector abundances. It is worth mentioning that the assumption of thermal equilibrium of sterile neutrino is important to realize such exponential growth [55]. For the benchmark point, the DM abundance Y_χ is much larger than the dark scalar abundance Y_ϕ, so the contribution from delayed decay $\phi \to \chi\nu$ to the total Y_χ is not obvious. Naturally, the ratio R_χ exponentially increases to $R_\chi^{\max} \simeq 1.9 \times 10^5$ until the end of the semiproduction

TABLE V. The parameter choices for the four cases in scenario 4, the units of masses involved are GeV.

Scenario 4	m_χ	m_ϕ	m_N	y_N	y_χ	$\lvert y_{\nu 1}\rvert$	$\lambda_{H\phi}$	μ	$\mathrm{Im}(\xi)$
a	10	25	30	10^{-13}	10^{-12}	7×10^{-7}	4.8×10^{-12}	25	1.78
b	10	25	30	10^{-13}	1.2×10^{-4}	5×10^{-6}	3.9×10^{-12}	25	3.72
c	10	25	30	1.2×10^{-7}	10^{-12}	8×10^{-7}	10^{-14}	25	1.91
d	10	25	30	1.7×10^{-7}	1.2×10^{-4}	10^{-6}	10^{-14}	25	2.12

processes. Afterwards R_χ is affected by $\phi\to\chi\nu$, and finally decreases to 8.2×10^4 in scenario 3(c).

In scenario 3(d), we reduce the value of y_N, so Y_χ will eventually fail to satisfy the observed relic density even with the enhancement by the semiproduction processes $N\chi\to\phi\phi$ and $N\phi\to\phi\chi$ as in scenario 3(c). On the other hand, y_χ is taken as a large value 5.7×10^{-1}, which then increases the third semiproduction processes $N\chi\to\chi\chi$ with $\langle\sigma v\rangle_{N\chi\to\chi\chi}\simeq3.5\times10^{-35}\ \mathrm{cm}^3/\mathrm{s}$. The new semiproduction process $N\chi\to\chi\chi$ will cause an additional contribution to the exponential growth of Y_χ to satisfy the Planck constraint. Meanwhile, the cross section of the conversion process $\phi\phi\to\chi\chi$ is greatly enhanced to about $8.5\times10^{-21}\ \mathrm{cm}^3/\mathrm{s}$, which makes an equal amount of Y_ϕ and Y_χ when $z\lesssim1$. Afterward, the conversion process quickly converts the dark scalar into DM. The ratio R_χ

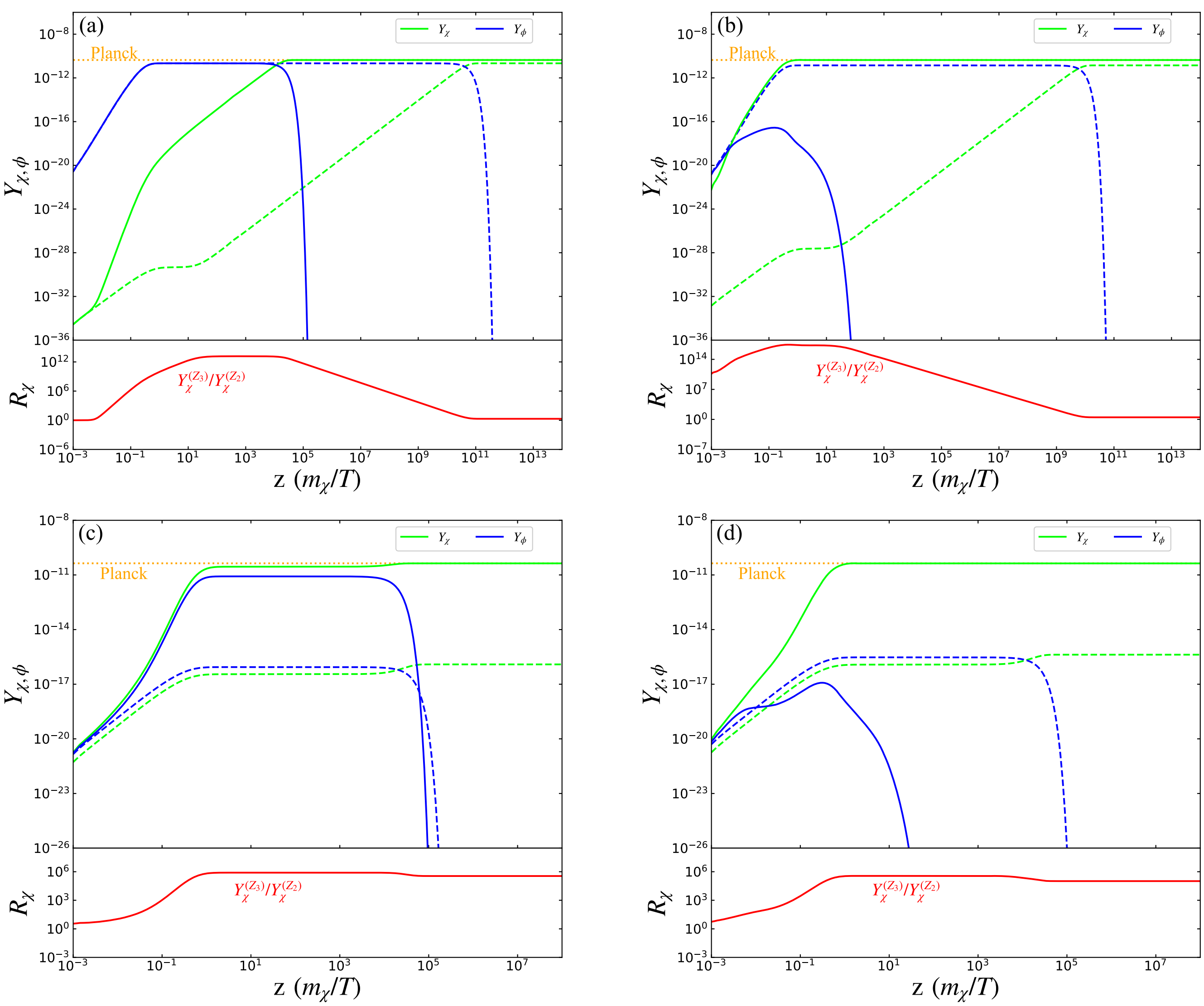

FIG. 6. Same as Fig. 3, but for scenario 4. Panels (a), (b), (c) and (d) correspond to the four cases in Table V respectively

exponentially increases to $R_\chi^{\max} \simeq 7.7 \times 10^6$, and R_χ finally decreases to 3.2×10^6.

The former two cases in scenario 3 indicate that when the DM abundance is dominant by the delayed decay $\phi \to \chi\nu$, the predicted final DM abundances of Z_2 and Z_3 are the same. However, when DM is primarily generated through the neutrino portal scattering process $NN \to \chi\chi$ and $h\nu \to \phi\chi$, the semiproduction processes $N\chi \to \phi\phi$, $N\phi \to \phi\chi$ and $N\chi \to \chi\chi$ could lead to the exponential growth of the dark sector abundances. The latter two cases in scenario 3 have quite different predictions between the Z_2 and Z_3 symmetric models, and thus are useful to distinguish these two models.

D. Scenario 4

Scenario 4 has also opened the pair decay $\phi \to \chi\chi$ in contrast with scenario 3. Besides the final decay mode of dark scalar ϕ, the initial generation channels of the dark sector in scenario 4 are consistent with that in scenario 3. Table V and Fig. 6 correspond to the selection of parameters and the evolution of dark abundances, respectively.

In scenario 4(a), the dark scalar ϕ is produced via the Higgs portal SM $\to \phi\phi$ process. Productions from $2 \to 2$ scattering processes are quite inefficient, and the DM χ is generated by the fast pair decay $\phi \to \chi\chi$ under the Z_3 symmetry. Compared with scenario 3(a), a slightly smaller $\lambda_{H\phi}$ is enough to realize the correct DM relic abundance, which is also due to the pair decay. This decay can lead to the ratio R_χ increasing to $\mathcal{O}(10^{13})$, and then decrease to two finally.

In scenario 4(b), both the conversion process $\phi\phi \to \chi\chi$ and decay $\phi \to \chi\chi$ are greatly enhanced. Same as in scenario 2(b), these two processes lead to more efficient production of DM than scenario 4(a), so a smaller $\lambda_{H\phi}$ in this scenario is enough to produce correct DM abundance. The ratio R_χ quickly reaches the maximum value of $\sim 10^{17}$, then gradually decreases to 3.1.

In scenario 4(c), the dark sector abundances are first generated by the $2 \to 2$ scattering processes with typical cross section $\langle\sigma v\rangle_{NN\to\phi\phi} \simeq 5 \times 10^{-49}$ cm^3/s, $\langle\sigma v\rangle_{NN\to\chi\chi} \simeq 1.7 \times 10^{-49}$ cm^3/s, and $\langle\sigma v\rangle_{h\nu\to\chi\phi} \simeq 2.7 \times 10^{-49}$ cm^3/s for the benchmark point. Then the relatively large semiproduction processes $N\chi \to \phi\phi$ and $N\phi \to \phi\chi$ exponentially enhance the dark sector abundances. The ratio R_χ exponentially increases to 8×10^5, and is further enlarged by the pair decay $\phi \to \chi\chi$. Finally R_χ decreases to 3.5×10^5 due to the delayed contribution of $\phi \to \chi\nu$ under the Z_2 symmetry.

In scenario 4(d), the large pair decay width $\Gamma_{\phi\to\chi\chi}$ makes the dark scalar ϕ quite short lived. The produced dark scalar rapidly decays into the DM pair, rather than taking part in the semiproduction processes $N\chi \to \phi\phi$ and $N\phi \to \phi\chi$, which clearly weakens the exponential enhancement effect. Therefore, a larger y_N is required to produce the observed DM abundance compared with scenario 4(c). The ratio R_χ exponentially increases to 3.6×10^5, then decreases to 1×10^5 finally.

Similar to scenario 2, the pair decay $\phi \to \chi\chi$ is more efficient in producing DM abundance in the Z_3 symmetric model even when the dark scalar is generated through the Higgs portal SM $\to \phi\phi$. Exponential enhancement by the semiproduction processes $N\chi \to \phi\phi$ and $N\phi \to \phi\chi$ are also possible in this scenario. However, the rapid pair decay $\phi \to \chi\chi$ may weaken the enhancement effect.

IV. PHENOMENOLOGY

The sterile neutrino portal FIMP DM model has rich phenomenology [70]. Despite the DM χ being hard to detect, both the sterile neutrino N and dark scalar ϕ lead to observable signatures. The sterile neutrino N can be directly produced at colliders [24]. Meanwhile, the neutrino from delayed decay $\phi \to \chi\nu$ affects the cosmic microwave background (CMB), the energetic neutrino spectrum, and the effective number of relativistic neutrino species [70].

The collider signatures of sterile neutrino N will be analyzed briefly. The electroweak scale N can be produced at large hadron collider (LHC) via the process $pp \to W \to \ell^\pm N$. The cross section of this process is determined by the mixing matrix θ. Lepton number violation signature arises from the decay $N \to \ell^\pm W^\mp \to \ell^\pm q_1 \bar{q}_2$ [71]. When $m_N < m_W$, the three-body decay via off-shell W/Z is the dominant channel, which leads to the displaced vertex signature [72]. In Fig. 7(a), we summarize the status and future prospect of N. It should be noted that the collider signature of sterile neutrino N is flavor dependent. Here, we take the muon mixing $\theta_{\mu 1}$ for illustration. By searching for the displaced vertex signature, a quite large part of the parameter space with $m_N < m_W$ can be covered in the future. For our benchmark scenarios, they are all located in the allowed parameter space, and are within the reach of future colliders. Among them, scenarios 1(a) and 3(a) have a particularly large mixing angle to avoid being excluded by $N_{\rm eff}$.

Then we will focus on the cosmological constraints on $\phi \to \chi\nu$ in different scenarios under the Z_3 symmetry. The secondary particles emitted by the neutrino from delayed decay $\phi \to \chi\nu$ have a great impact on the CMB anisotropies and spectral distortions. In Fig. 7(b), we show the corresponding cosmological constraints, where the fractional abundance $f_\phi = \Omega_\phi/\Omega_{\rm DM}$, $\varepsilon = (m_\phi^2 - m_\chi^2)/2m_\phi^2$ denotes the fraction of the energy of ϕ that has been transferred to neutrinos [81].

In scenario 1, the typical lifetime of dark scalar τ_ϕ is about 10^9–10^{12} s with the tiny coupling $y_N \sim 10^{-13}$–10^{-12}. The benchmark points have relatively large values of $f_\phi \varepsilon \gtrsim \mathcal{O}(10^{-3})$. In contrast, the benchmark points in scenario 2 have much smaller values of $f_\phi \varepsilon$ due to tiny branching ratio of $\phi \to \chi\nu$. The lifetimes are $\tau_\phi \sim 10^1$ s in

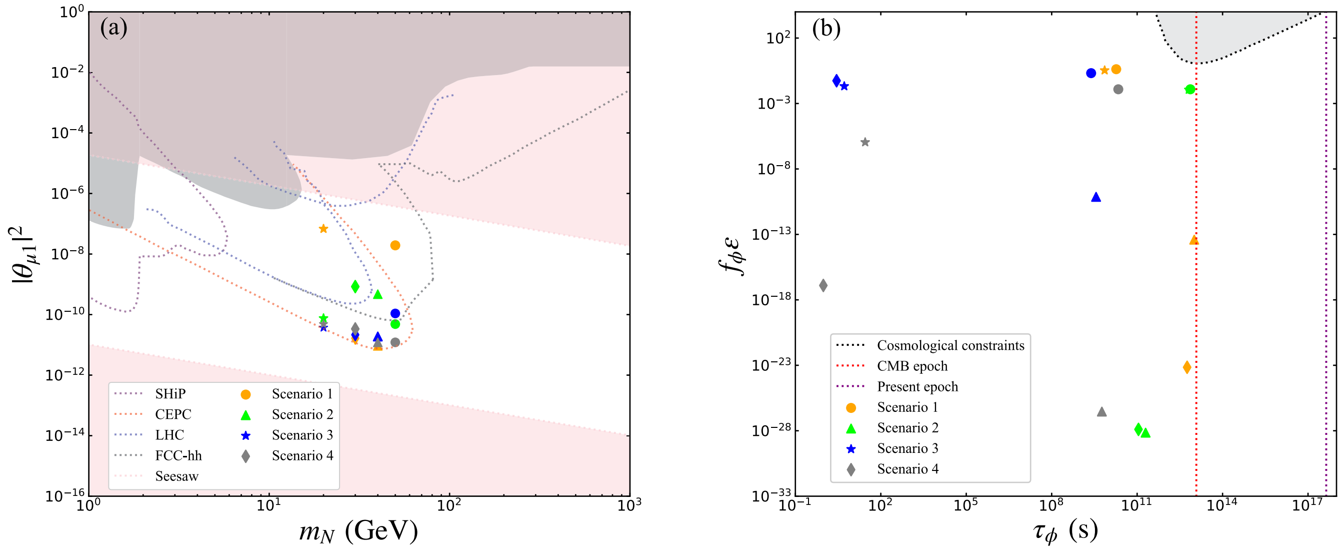

FIG. 7. Status and future prospect of sterile neutrino N (panel a). The gray areas have been excluded by current experiments [73]. The purple, red, blue, and black dotted lines are the future limits from SHiP [74,75], CEPC [76], LHC [77,78], and FCC-hh [79], respectively. The pink regions are disfavored by the neutrino oscillation and lepton flavor violation [62]. Cosmological constraints of dark scalar ϕ (panel b). In panel b, the black dotted line represents the cosmological constraint discussed in [80] with $m_\phi = 10$ GeV, and the red and purple dotted lines represent the two epochs of CMB and present, respectively. The circle, triangle, star, and diamond represent scenarios 1 to 4. Meanwhile, the orange, green, blue, and gray samples represent the four cases (a) to (d) for each scenario. Scenario 1(b) and 3(b) predict very close results, thus are overlapped in the figure.

scenarios 3(c) and 3(d), which are much smaller than that in cases (a) and (b). Meanwhile scenario 3(d) has a much smaller value of $f_\phi \varepsilon$, which is caused by the rapid conversion of $\phi\phi \to \chi\chi$. Scenario 4 has similar τ_ϕ values with scenario 3. Scenario 4(c) has a relative larger $f_\phi \varepsilon$ because of the large branching ratio of $\phi \to \chi\nu$. As shown in Ref. [80], the fraction of injected electromagnetic energy is heavily suppressed when $m_\phi < m_W$. So all the benchmark points in these study can easily satisfy the cosmological constraints.

The energetic neutrinos generated by the delayed decay of ϕ will be captured by current neutrino experiments. The neutrino flux at present is calculated as [47]

$$\Phi_{\rm cos} \equiv E_\nu \frac{d\varphi}{dE_\nu} = \left(\frac{n_\phi}{\tau_\phi}\right)\left(\frac{e^{-t(x)/\tau_\phi}}{H(x)}\right)\theta'(x), \qquad (15)$$

where E_ν is the observed neutrino energy, $d\varphi/dE_\nu$ is the predicted neutrino flux, n_ϕ is the number density of ϕ if it is stable, and $\theta'(x)$ is the Heaviside theta function. The cosmic time $t(x)$ at red-shift $1+x$ and the Hubble parameter $H(x)$ in the standard cosmology are given by

$$t(x) \approx \frac{4}{3H_0}\left(\frac{\Omega_{\rm r}^{3/2}}{\Omega_{\rm m}^2}\right)\left(1 - \left(1 - \frac{\Omega_{\rm m}}{2(1+x)\Omega_{\rm r}}\right) \times \sqrt{1 + \frac{\Omega_{\rm m}}{(1+x)\Omega_{\rm r}}}\right), \qquad (16)$$

$$H(x) = H_0\sqrt{\Omega_\Lambda + (1+x)^3\Omega_{\rm m} + (1+x)^4\Omega_{\rm r}}, \qquad (17)$$

where $x = E_0/E_\nu - 1$ with initial energy $E_0 = (m_\phi^2 - m_\chi^2)/2m_\phi$, the Hubble constant $H_0 = 100h$ km/s/Mpc with $h = 0.6727$ [69]. The dark energy, matter, and radiation fractions are $\Omega_\Lambda = 0.6846$, $\Omega_{\rm m} = 0.315$ and $\Omega_{\rm r} = 9.265 \times 10^{-5}$, respectively.

It should be noted that the neutrino fluxes from $\phi \to \chi\nu$ heavily depend on the dark scalar number density n_ϕ. Provided the same parameters for both Z_2 and Z_3 symmetry, the relic density of Z_2 symmetry usually cannot satisfy the observed value, which makes the corresponding predictions less promising. In the following discussion, we also modify certain parameters of Z_2 symmetry to predict correct relic density. The neutrino fluxes generated in the four scenarios are shown in Fig. 8, where both results of the Z_2 and Z_3 symmetry are shown.

Scenarios 1(a) and 1(c) cannot be distinguished by neutrino fluxes in both symmetries; however, the neutrino fluxes of scenarios 1(b) and 1(d) in Z_2 symmetry are slightly higher than that in Z_3 symmetry. Four cases of scenario 2 in Z_3 symmetry have tiny n_ϕ, which means that they will generate very weak neutrino flux, and thus are not shown in the figure. Meanwhile, case 2(a) in the Z_2 symmetry is excluded by the current experiment. In scenario 3, the distinctions between (a) and (b) under two symmetries are similar to that in scenario 1. The predicted neutrino fluxes for scenarios 3(c) and 3(d) are difficult to detect by current

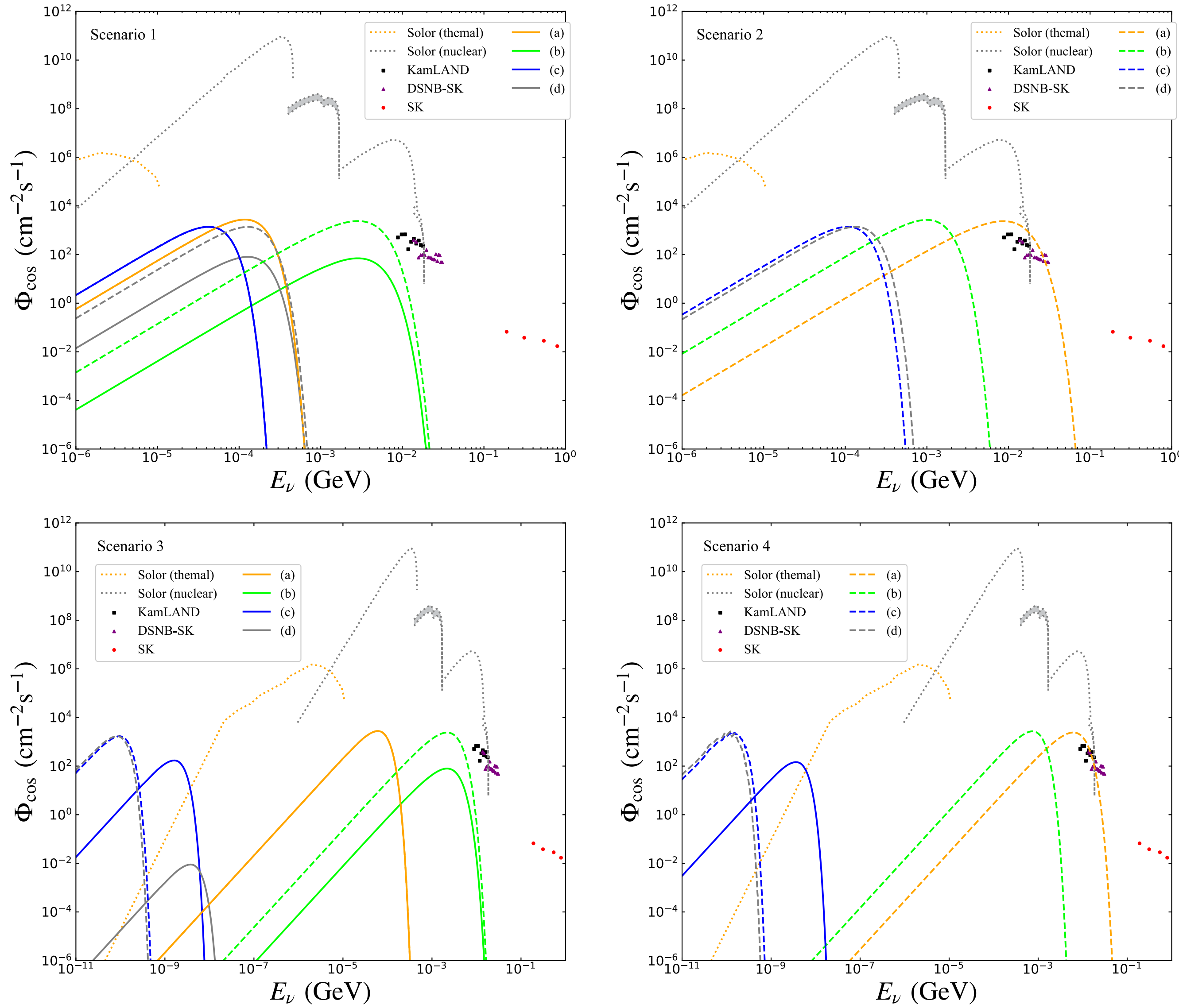

FIG. 8. The predicted neutrino fluxes at present for the benchmark scenarios. The yellow and gray dotted lines are the thermal and nuclear solar neutrino flux [82]. The black squares and purple triangles represent the 90% C.L. upper limits of the diffuse supernova neutrino background (DSNB) flux by the KamLAND [83] and SK [84], respectively. The red points are the atmospheric neutrino data from SK [85]. The orange, green, blue, and gray solid lines correspond to cases (a), (b), (c), and (d) for each scenario, while solid and dashed lines correspond to Z_3 and Z_2 scenarios, respectively.

experiments, despite existing a significant differences between the Z_2 and Z_3 symmetries. Compared to scenario 2, scenario 4(c) in the Z_3 symmetry has a large neutrino flux, but the neutrino energy is too low to be detected. Only scenario 4(a) in the Z_2 symmetry is excluded.

The neutrinos generated from $\phi \to \chi\nu$ also increase the effective number of relativistic neutrino species $N_{\rm eff}$, which can be written as

$$N_{\rm eff} = \frac{7}{8}\left(\frac{11}{4}\right)^{4/3}\left(\frac{\rho_\nu}{\rho_\gamma}\right) = 3\left(\frac{11}{4}\right)^{4/3}\left(\frac{T_\nu}{T_\gamma}\right)^4, \quad (18)$$

where ρ_ν and ρ_γ represent the energy densities of light neutrinos and photons, respectively, and T_ν and T_γ are their corresponding temperatures. By modifying the evolution equations of T_ν and T_γ in SM [86,87], the corresponding equations that conform to our model are

$$\frac{dT_\gamma}{dt} = -\frac{4H\rho_\gamma + 3H(\rho_e + p_e) + \frac{\delta\rho_{\nu_e}}{\delta t} + 2\frac{\delta\rho_{\nu_\mu}}{\delta t} - \varepsilon\xi_{\rm EM}\frac{\rho_\phi}{\tau_\phi}}{\frac{\partial\rho_\gamma}{\partial T_\gamma} + \frac{\partial\rho_e}{\partial T_\gamma}}, \quad (19)$$

$$\frac{dT_\nu}{dt} = -HT_\nu + \frac{\frac{\delta\rho_{\nu_e}}{\delta t} + 2\frac{\delta\rho_{\nu_\mu}}{\delta t} + \varepsilon(1-\xi_{\rm EM})\frac{\rho_\phi}{\tau_\phi}}{3\frac{\partial\rho_\nu}{\partial T_\nu}}. \quad (20)$$

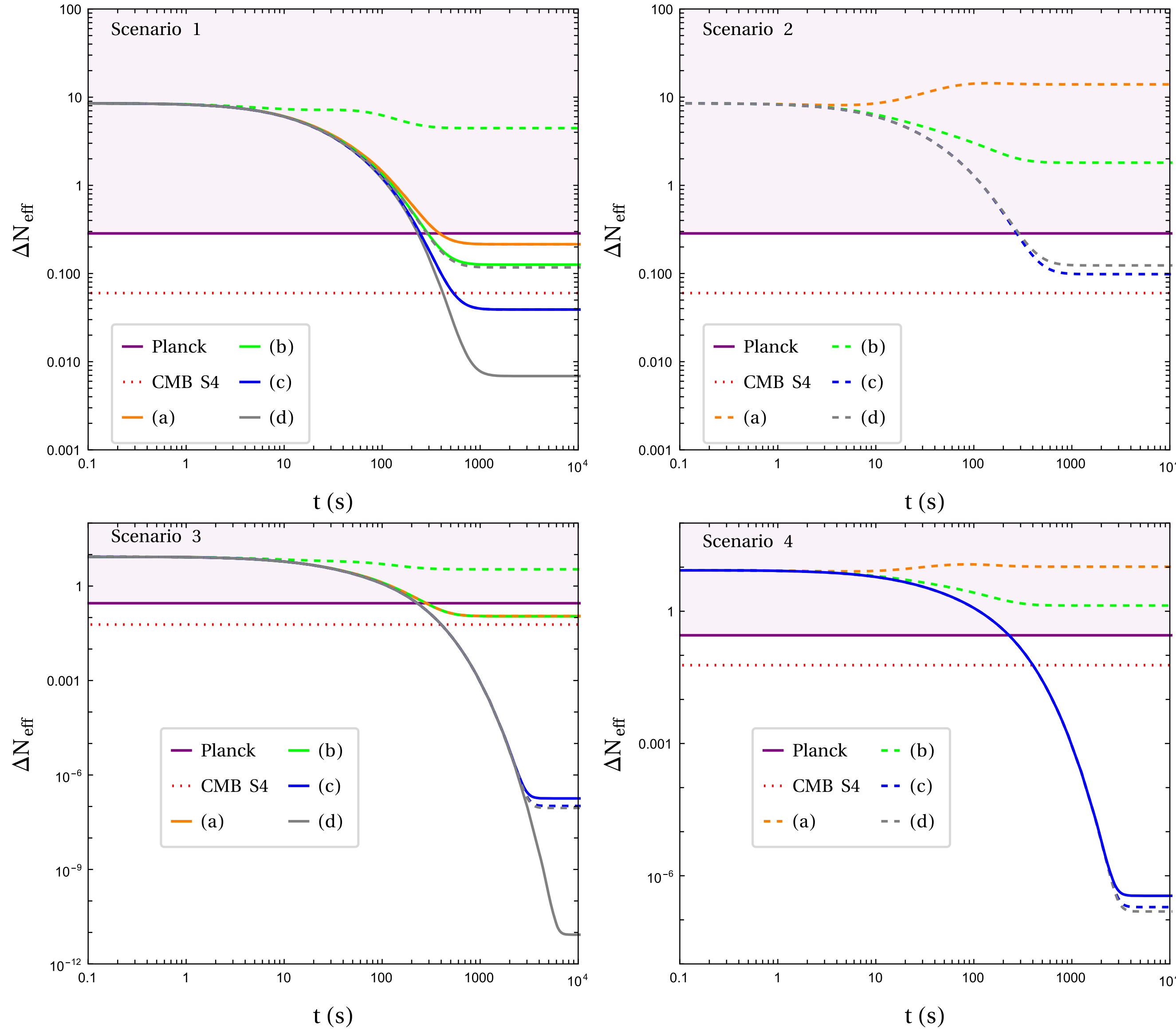

FIG. 9. The evolution of ΔN_{eff} for the four benchmark scenarios. The calculations are started at $T_\gamma = T_\nu = 10$ MeV with the corresponding initial time $t_0 = \frac{1}{2H}|_{\mathrm{T=10\ MeV}}$. The purple solid and red dotted lines represent the constraints of ΔN_{eff} from current Planck [69] and future CMB S4 [91], respectively. The orange, green, blue, and gray solid lines correspond to cases (a), (b), (c), and (d) for each scenario, while solid and dashed lines correspond to Z_3 and Z_2 scenarios respectively.

where $\rho_{\gamma,e,\nu}$ denote the energy densities of γ, e, and ν. ρ_ϕ expresses the energy density of ϕ provided it is stable. p_e is the pressure density of e. ξ_{EM} represents the energy fraction that the neutrinos inject into electromagnetic plasma, which is assumed to be zero for the selection of m_ϕ in this work [80]. The neutrino-electron energy density transfer rate $\delta\rho_\nu/\delta t$ is taken from Refs. [86,87]. In addition, we do not distinguish the flavor of neutrinos here.

The evolution of ΔN_{eff} for scenarios 1–4 are shown in Fig. 9, here $\Delta N_{\mathrm{eff}} \equiv N_{\mathrm{eff}} - N_{\mathrm{eff}}^{\mathrm{SM}}$ with $N_{\mathrm{eff}}^{\mathrm{SM}} = 3.045$ [88–90]. For scenario 1(a), the predicted values of ΔN_{eff} are the same for the Z_2 and the Z_3 symmetries, which can be tested by the future CMB S4 experiment. For scenario 1(b), the value of ΔN_{eff} in the Z_2 symmetry is already excluded by Planck, while it is still allowed in the Z_3 symmetry. For scenario 1(c), both symmetries lead to ΔN_{eff} beyond the reach of CMB S4. For scenario 1(d), the Z_2 symmetry can be probe by CMS S4, but the Z_3 symmetry can not. For scenario 2, the branching ratios of $\phi \to \chi\nu$ in the Z_3 symmetry are heavily suppressed since the $\phi \to \chi\chi$ decay is allowed. So the predicted values of ΔN_{eff} in the Z_3 symmetry are extremely small, and thus are not shown in the figure. For scenario 2 with the Z_2 symmetry, cases (a) and (b) are excluded by current experiment, meanwhile cases (c) and (d) are within the reach of future CMB S4.

Scenarios 3(a) and 3(b) in the Z_3 symmetry, as well as 3(a) in the Z_2 symmetry, have almost identical results, which are allowed by the Planck constraint and can be further excluded by CMB S4. Scenario 3(b) in the Z_2 symmetry is already disallowed by current limit. Scenarios 3(c) and 3(d) in both symmetries have small $\Delta N_{\rm eff}$, which are much lower than CMB S4 bound. For scenario 4, cases (a) and (b) in the Z_2 symmetry are excluded, while other cases all predict tiny $\Delta N_{\rm eff}$.

V. DISCUSSION AND CONCLUSION

The feeble sterile neutrino portal DM with Z_3 symmetry is studied in this paper. Besides the sterile neutrino N, a dark sector with one fermion singlet χ and one scalar singlet ϕ is also introduced. The dark sector ϕ and χ are charged under a Z_3 symmetry. In addition to the well-studied sterile neutrino portal Yukawa coupling $y_N \phi \bar{\chi} N$ and Higgs portal coupling $\lambda_{H\phi}(H^\dagger H)(\phi^\dagger \phi)$ in the Z_2 symmetric model, the Z_3 symmetry further allows the dark sector Yukawa interaction $y_\chi \phi \overline{\chi^c} \chi$ and dark scalar self-interaction $\mu\phi^3/2$. Provided the fermion singlet χ as the FIMP DM candidate, the latter two terms could generate new production channels for DM in the Z_3 symmetric model.

Because various production channels depend on the mass spectrum, we consider four specific scenarios to illustrate the evolution of the dark sector. We find that the dominant production and decay mode of dark scalar ϕ has a great effect on the evolution of DM. When the delayed decay $\phi \to \chi\nu$ is the only decay mode of ϕ, the dark scalar generated from the Higgs portal process SM $\to \phi\phi$ [as in scenarios 1(a), 1(b), 3(a), 3(b)] or from direct decay $N \to \phi\chi$ [as in scenarios 1(c), 1(d)] will lead to the same final DM abundance for both Z_2 and Z_3 symmetry. For scenarios 1(a), 1(c), and 3(a), both Z_2 and Z_3 symmetries lead to the same phenomenological results, and thus cannot be distinguished. The conversion process $\phi\phi \to \chi\chi$ could alert the fractional abundance f_ϕ in the Z_3 symmetric model, which causes scenarios 1(b), 1(d), and scenario 3(b) to have differences in neutrino flux $\Phi_{\rm cos}$ and additional effective neutrino species $\Delta N_{\rm eff}$ under different symmetries. The most promising scenarios in the Z_3 model are 1(b) and 3(b), which can be tested at future CMB S4. Meanwhile, the corresponding scenarios 1(b) and 3(b) in the Z_2 model have already been excluded. For scenario 1(d), if the future CMB S4 observes relatively large $\Delta N_{\rm eff}$, then the Z_3 symmetry is disfavored.

When the pair decay $\phi \to \chi\chi$ is kinematically allowed, it becomes the dominant decay mode of dark scalar, since the delayed decay $\phi \to \chi\nu$ is heavily suppressed by the tiny mixing angle in our analysis. This pair decay $\phi \to \chi\chi$ only appears in the Z_3 symmetric model, and thus definitely leads to a difference between the two kinds of symmetric models. When the dark scalar is dominantly produced from the Higgs portal process SM $\to \phi\phi$ [as in scenarios 2(a), 2(b), 4(a), 4(b)], the final DM abundance in the Z_3 symmetry is at least twice as large as it in the Z_2 symmetry. Meanwhile, if the dark scalar is generated from the direct decay $N \to \phi\chi$ [as in scenarios 2(c), 2(d)], the DM relic abundance ratio of the Z_3 symmetry to the Z_2 symmetry is three to two. In short, the pair decay is more efficient in producing DM. With a suppressed branching ratio of $\phi \to \chi\nu$, these scenarios are easily to avoid the cosmological constraints, but are also hard to be tested even at future experiments. However, the corresponding scenarios in the Z_2 symmetry usually predict large neutrino flux and $\Delta N_{\rm eff}$, which can all be excluded by future CMB S4. If no excess is observed in the future, we conclude that the Z_3 symmetry is favored, but is hard to confirm.

The most interesting scenario is when the dark sector is primarily generated by the scattering processes as $NN \to \chi\chi, NN \to \phi\phi, h\nu \to \chi\phi$ [as in scenarios 3(c), 3(d), 4(c), 4(d)]. Then the semiproduction process $N\chi \to \phi\phi, N\phi \to \phi\chi, N\chi \to \chi\chi$ could lead to the exponential growth of dark sector abundances in the Z_3 symmetric model. Compared with the Z_2 symmetric model, the final DM abundance of such scenarios could be enhanced by 5 to 6 orders of magnitudes. Our benchmark points also indicate that the generation of DM χ is much more efficient than the dark scalar, which results in a tiny fractional abundance f_ϕ. Meanwhile, the relatively large Yukawa coupling $y_N \sim \mathcal{O}(10^{-7})$ significantly reduces the lifetime of the dark scalar ϕ. These two aspects make such scenarios hard to

TABLE VI. Discrepancy between Z_2 and Z_3 symmetric models.

		Scenario 1	Scenario 2	Scenario 3	Scenario 4
Symmetry	Phenomenology	a, b, c, d	a, b, c, d	a, b, c, d	a, b, c, d
Z_2	Relic Density	✓✓✓✓	✗✗✗✗	✓✓✗✗	✗✗✗✗
	Neutrino Flux	✓✓✓✓	✗✓✓✓	✓✓✓✓	✗✓✓✓
	$N_{\rm eff}$ Planck	✓✗✓✓	✗✗✓✓	✓✗✓✓	✗✗✓✓
	$N_{\rm eff}$ CMB S4	✗✗✓✗	✗✗✗✗	✗✗✓✓	✗✗✓✓
Z_3	Relic Density	✓✓✓✓	✓✓✓✓	✓✓✓✓	✓✓✓✓
	Neutrino Flux	✓✓✓✓	✓✓✓✓	✓✓✓✓	✓✓✓✓
	$N_{\rm eff}$ Planck	✓✓✓✓	✓✓✓✓	✓✓✓✓	✓✓✓✓
	$N_{\rm eff}$ CMB S4	✗✗✓✓	✓✓✓✓	✗✗✓✓	✓✓✓✓

probe via the cosmological observables, even when $\phi \to \chi\nu$ is the only decay mode. Therefore, except for differences in the predicted values of relic abundances, we cannot distinguish the Z_2 and Z_3 symmetries via the cosmological observables for these scenarios.

The phenomenological signals corresponding to the 16 cases for both Z_2 and Z_3 symmetry are summarized in Table VI. The collider signature of sterile neutrino only depends on the mass m_N and mixing angle θ, which are the same for both Z_2 and Z_3 symmetries. Therefore, the collider signatures are not listed in Table VI. As shown in Fig. 7, all benchmark points satisfy cosmological constraints from CMB, so they are not shown in Table VI either. Because some scenarios are hard to test via cosmological observables, we choose benchmark points that all can be tested at future colliders, which require the mixing matrix θ much larger than the seesaw low limit.

There are discrepancies of favored parameter space for different phenomenological variables. For example, the relatively large mixing matrix θ is favored by collider searches, but it will lead to the lifetime τ_ϕ smaller, which weakens the impact of delayed decay $\phi \to \chi\nu$ on cosmological observables. For a small mixing matrix θ at the natural seesaw predict scale, the Z_2 model is strongly disfavored by cosmological observables [70]. Meanwhile, some scenarios with suppressed contribution of $\phi \to \chi\nu$ in the Z_3 model can still satisfy all the cosmological constraints.

ACKNOWLEDGMENTS

This work is supported by the National Natural Science Foundation of China under Grants No. 12375074, No. 11805081, and No. 11635009, Natural Science Foundation of Shandong Province under Grants No. ZR2019QA021 and No. ZR2022 MA056, the Open Project of Guangxi Key Laboratory of Nuclear Physics and Nuclear Technology under Grant No. NLK2021-07.

[1] G. Aad *et al.* (ATLAS Collaboration), Phys. Lett. B **716**, 1 (2012).
[2] S. Chatrchyan *et al.* (CMS Collaboration), Phys. Lett. B **716**, 30 (2012).
[3] T. Kajita, Rev. Mod. Phys. **88**, 030501 (2016).
[4] A. B. McDonald, Rev. Mod. Phys. **88**, 030502 (2016).
[5] G. Bertone and D. Hooper, Rev. Mod. Phys. **90**, 045002 (2018).
[6] L. M. Krauss, S. Nasri, and M. Trodden, Phys. Rev. D **67**, 085002 (2003).
[7] T. Asaka, S. Blanche, and M. Shaposhnikov, Phys. Lett. B **631**, 151 (2005).
[8] E. Ma, Phys. Rev. D **73**, 077301 (2006).
[9] M. Aoki, S. Kanemura, and O. Seto, Phys. Rev. Lett. **102**, 051805 (2009).
[10] Y. Cai, J. Herrero-García, M. A. Schmidt, A. Vicente, and R. R. Volkas, Front. Phys. **5**, 63 (2017).
[11] P. Minkowski, Phys. Lett. **67B**, 421 (1977).
[12] R. N. Mohapatra and G. Senjanovic, Phys. Rev. Lett. **44**, 912 (1980).
[13] S. Dodelson and L. M. Widrow, Phys. Rev. Lett. **72**, 17 (1994).
[14] M. Drewes, T. Lasserre, A. Merle, S. Mertens, R. Adhikari, M. Agostini, N. A. Ky, T. Araki, M. Archidiacono, M. Bahr *et al.*, J. Cosmol. Astropart. Phys. 01 (2017) 025.
[15] A. Datta, R. Roshan, and A. Sil, Phys. Rev. Lett. **127**, 231801 (2021).
[16] A. Das, S. Goswami, K. N. Vishnudath, and T. K. Poddar, arXiv:2104.13986.
[17] K. C. Y. Ng, B. M. Roach, K. Perez, J. F. Beacom, S. Horiuchi, R. Krivonos, and D. R. Wik, Phys. Rev. D **99**, 083005 (2019).
[18] E. Ma, Phys. Lett. B **662**, 49 (2008).
[19] A. Das, S. Gola, S. Mandal, and N. Sinha, Phys. Lett. B **829**, 137117 (2022).
[20] M. Hirsch, R. A. Lineros, S. Morisi, J. Palacio, N. Rojas, and J. W. F. Valle, J. High Energy Phys. 10 (2013) 149.
[21] S. Davidson and A. Ibarra, Phys. Lett. B **535**, 25 (2002).
[22] F. Vissani, Phys. Rev. D **57**, 7027 (1998).
[23] T. Han and B. Zhang, Phys. Rev. Lett. **97**, 171804 (2006).
[24] A. M. Abdullahi, P. B. Alzas, B. Batell, J. Beacham, A. Boyarsky, S. Carbajal, A. Chatterjee, J. I. Crespo-Anadon, F. F. Deppisch, A. De Roeck *et al.*, J. Phys. G **50**, 020501 (2023).
[25] M. Escudero, N. Rius, and V. Sanz, J. High Energy Phys. 02 (2017) 045.
[26] M. Escudero, N. Rius, and V. Sanz, Eur. Phys. J. C **77**, 397 (2017).
[27] M. D. Campos, F. S. Queiroz, C. E. Yaguna, and C. Weniger, J. Cosmol. Astropart. Phys. 07 (2017) 016.
[28] B. Batell, T. Han, and B. Shams Es Haghi, Phys. Rev. D **97**, 095020 (2018).
[29] B. Batell, T. Han, D. McKeen, and B. Shams Es Haghi, Phys. Rev. D **97**, 075016 (2018).
[30] M. Blennow, E. Fernandez-Martinez, A. Olivares-Del Campo, S. Pascoli, S. Rosauro-Alcaraz, and A. V. Titov, Eur. Phys. J. C **79**, 555 (2019).
[31] E. Hall, T. Konstandin, R. McGehee, and H. Murayama, Phys. Rev. D **107**, 055011 (2023).
[32] L. Coito, C. Faubel, J. Herrero-García, A. Santamaria, and A. Titov, J. High Energy Phys. 08 (2022) 085.
[33] J. L. Feng, Annu. Rev. Astron. Astrophys. **48**, 495 (2010).
[34] L. Roszkowski, E. M. Sessolo, and S. Trojanowski, Rep. Prog. Phys. **81**, 066201 (2018).
[35] M. Schumann, J. Phys. G **46**, 103003 (2019).

[36] G. Arcadi, M. Dutra, P. Ghosh, M. Lindner, Y. Mambrini, M. Pierre, S. Profumo, and F. S. Queiroz, Eur. Phys. J. C **78**, 203 (2018).
[37] E. Aprile *et al.* (XENON Collaboration), Phys. Rev. Lett. **121**, 111302 (2018).
[38] E. Aprile *et al.* (XENON Collaboration), Phys. Rev. Lett. **131**, 041003 (2023).
[39] X. Cui *et al.* (PandaX-II Collaboration), Phys. Rev. Lett. **119**, 181302 (2017).
[40] Y. Meng *et al.* (PandaX-4T Collaboration), Phys. Rev. Lett. **127**, 261802 (2021).
[41] A. Boveia and C. Doglioni, Annu. Rev. Nucl. Part. Sci. **68**, 429 (2018).
[42] W. Adam and I. Vivarelli, Int. J. Mod. Phys. A **37**, 2130022 (2022).
[43] M. Aguilar *et al.* (AMS Collaboration), Phys. Rev. Lett. **110**, 141102 (2013).
[44] M. Ackermann *et al.* (Fermi-LAT Collaboration), Phys. Rev. Lett. **115**, 231301 (2015).
[45] L. J. Hall, K. Jedamzik, J. March-Russell, and S. M. West, J. High Energy Phys. 03 (2010) 080.
[46] N. Bernal, M. Heikinheimo, T. Tenkanen, K. Tuominen, and V. Vaskonen, Int. J. Mod. Phys. A **32**, 1730023 (2017).
[47] P. Bandyopadhyay, E. J. Chun, and R. Mandal, J. Cosmol. Astropart. Phys. 08 (2020) 019.
[48] Y. Cheng and W. Liao, Phys. Lett. B **815**, 136118 (2021).
[49] A. Falkowski, E. Kuflik, N. Levi, and T. Volansky, Phys. Rev. D **99**, 015022 (2019).
[50] A. Liu, Z. L. Han, Y. Jin, and F. X. Yang, Phys. Rev. D **101**, 095005 (2020).
[51] Z. F. Chang, Z. X. Chen, J. S. Xu, and Z. L. Han, J. Cosmol. Astropart. Phys. 06 (2021) 006.
[52] D. K. Ghosh, P. Ghosh, and S. Jeesun, J. Cosmol. Astropart. Phys. 07 (2023) 012.
[53] P. Bandyopadhyay, D. Choudhury, and D. Sachdeva, Phys. Rev. D **107**, 015020 (2023).
[54] A. Liu, Z. L. Han, Y. Jin, and H. Li, Phys. Rev. D **108**, 075021 (2023).
[55] T. Bringmann, P. F. Depta, M. Hufnagel, J. T. Ruderman, and K. Schmidt-Hoberg, Phys. Rev. Lett. **127**, 19 (2021).
[56] A. Hryczuk and M. Laletin, J. High Energy Phys. 06 (2021) 026.
[57] T. Bringmann, P. F. Depta, M. Hufnagel, J. Kersten, J. T. Ruderman, and K. Schmidt-Hoberg, Phys. Rev. D **107**, L071702 (2023).
[58] G. Belanger, K. Kannike, A. Pukhov, and M. Raidal, J. Cosmol. Astropart. Phys. 01 (2013) 022.
[59] A. Hektor, A. Hryczuk, and K. Kannike, J. High Energy Phys. 03 (2019) 204.
[60] B. Barman, P. S. Bhupal Dev, and A. Ghoshal, Phys. Rev. D **108**, 035037 (2023).
[61] J. A. Casas and A. Ibarra, Nucl. Phys. **B618**, 171 (2001).
[62] P. S. Bhupal Dev, S. Goswami, and M. Mitra, Phys. Rev. D **91**, 113004 (2015).
[63] I. Esteban, M. C. Gonzalez-Garcia, M. Maltoni, T. Schwetz, and A. Zhou, J. High Energy Phys. 09 (2020) 178.
[64] S. P. Li and X. J. Xu, J. Cosmol. Astropart. Phys. 06 (2023) 047.
[65] P. Bandyopadhyay, M. Mitra, R. Padhan, A. Roy, and M. Spannowsky, J. High Energy Phys. 05 (2022) 182.
[66] G. Belanger, F. Boudjema, A. Pukhov, and A. Semenov, Comput. Phys. Commun. **185**, 960 (2014).
[67] E. W. Kolb and S. Wolfram, Nucl. Phys. **B172**, 224 (1980); **B195**, 542(E) (1982).
[68] D. Bhatia, arXiv:2308.09801.
[69] N. Aghanim *et al.* (Planck Collaboration), Astron. Astrophys. **641**, A6 (2020); **652**, C4(E) (2021).
[70] A. Liu, F. L. Shao, Z. L. Han, Y. Jin, and H. Li, Phys. Rev. D **108**, 115028 (2023).
[71] Y. Cai, T. Han, T. Li, and R. Ruiz, Front. Phys. **6**, 40 (2018).
[72] M. Drewes and J. Hajer, J. High Energy Phys. 02 (2020) 070.
[73] A. Blondel, C. B. Verhaaren, J. Alimena, M. Bauer, P. Azzi, R. Ruiz, M. Neubert, O. Mikulenko, M. Ovchynnikov, M. Drewes *et al.*, Front. Phys. **10**, 967881 (2022).
[74] C. Ahdida *et al.* (SHiP Collaboration), J. High Energy Phys. 04 (2019) 077.
[75] D. Gorbunov, I. Krasnov, Y. Kudenko, and S. Suvorov, Phys. Lett. B **810**, 135817 (2020).
[76] J. B. Guimarães da Costa *et al.* (CEPC Study Group Collaboration), arXiv:1811.10545.
[77] S. Pascoli, R. Ruiz, and C. Weiland, J. High Energy Phys. 06 (2019) 049.
[78] E. Izaguirre and B. Shuve, Phys. Rev. D **91**, 093010 (2015).
[79] S. Antusch, E. Cazzato, and O. Fischer, Int. J. Mod. Phys. A **32**, 1750078 (2017).
[80] T. Hambye, M. Hufnagel, and M. Lucca, J. Cosmol. Astropart. Phys. 05 (2022) 033.
[81] G. Blackadder and S. M. Koushiappas, Phys. Rev. D **90**, 103527 (2014).
[82] E. Vitagliano, I. Tamborra, and G. Raffelt, Rev. Mod. Phys. **92**, 045006 (2020).
[83] A. Gando *et al.* (KamLAND Collaboration), Astrophys. J. **745**, 193 (2012).
[84] H. Zhang *et al.* (Super-Kamiokande Collaboration), Astropart. Phys. **60**, 41 (2015).
[85] E. Richard *et al.* (Super-Kamiokande Collaboration), Phys. Rev. D **94**, 052001 (2016).
[86] M. Escudero Abenza, J. Cosmol. Astropart. Phys. 05 (2020) 048.
[87] M. Escudero, J. Cosmol. Astropart. Phys. 02 (2019) 007.
[88] G. Mangano, G. Miele, S. Pastor, T. Pinto, O. Pisanti, and P. D. Serpico, Nucl. Phys. **B729**, 221 (2005).
[89] E. Grohs, G. M. Fuller, C. T. Kishimoto, M. W. Paris, and A. Vlasenko, Phys. Rev. D **93**, 083522 (2016).
[90] P. F. de Salas and S. Pastor, J. Cosmol. Astropart. Phys. 07 (2016) 051.
[91] K. Abazajian, G. Addison, P. Adshead, Z. Ahmed, S. W. Allen, D. Alonso, M. Alvarez, A. Anderson, K. S. Arnold, C. Baccigalupi *et al.*, arXiv:1907.04473.